FEDERAL UNIVERSITY OF SÃO CARLOS - UFSCar
DEPARTMENT OF PHYSICS

Alexandre Jitsuo Fuzita

Anderson localization of light in two dimensions

São Carlos
2025

Alexandre Jitsuo Fuzita

Anderson localization of light in two dimensions

Dissertation presented to the Postgraduate Program in Physics of the Department of physics, Federal University of São Carlos to obtain the title of Master of physics.

Advisor: Prof. Dr. Romain Pierre Marcel Bachelard

São Carlos

2025

Acknowledgements

I would like to thank my advisor, Prof. Dr. Romain Pierre Marcel Bachelard, for the way he guided the development of this work, as well as for the opportunity and trust throughout my entire master's program.

I would also like to thank Dr. Carlos Eduardo Máximo for his support, discussions, and suggestions, which significantly enriched this work.

I would also like to thank Pada (Mateus), Rafael, Gubio, and Noel for supporting me during challenging moments and for always being willing to help.

I am grateful to the research group for all the enriching discussions, the support during our meetings, and their collaboration throughout my master's journey.

I would also like to thank the graduate students in the theoretical corridor of PPGF for the enjoyable moments that made this journey much lighter and more pleasant.

I am thankful to my family, who have always encouraged me to keep going, even in the most challenging times.

I would also like to thank Priscila Segur for all her support, patience, and for believing in me throughout this entire period. Her presence was essential in helping me overcome obstacles and achieve my goals.

Finally, I would like to thank the funding agencies CAPES and FAPESP for making this work possible.

"A educação transforma as pessoas.
As pessoas transformam o mundo."
Paulo Freire.

Abstract

Anderson localization is a physical phenomenon that occurs when waves propagate in disordered media. However, there is no conclusive observation of the existence of electromagnetic wave localization in three dimensions, most likely due to its vectorial nature. Interestingly, two-dimensional media possess both scalar and vector scattering channels for light, with localization in the former, and absence of localization in the latter where polarization effects must be taken into account. One characteristic of Anderson localization is the decay of the dimensionless conductance (also called Thouless number) with the system size ,according to the so-called scaling theory. For example, in a 2D dense system the vector channel has a conductance nearly constant with respect to the size of the system, whereas the scalar channel present an exponential decay. This work is devoted to studying the influence of the near-field and polarization coupling terms in the transport of 2D systems, in the limit of low density and large size. Indeed, the polarization-coupling term which prevent light localization in the vector channel is expected to be very weak, so localization may occur in this limit. We consider a two-dimensional circular cloud of point-like scatterers in a two-dimensional vacuum. Numerical simulations are realized to study the conductance as the system size increases, tuning the scatterers density. We present preliminary results on the scaling of the dimensionless conductance in the limit of decreasing densities, giving hints on the behaviour of localization in low-density 2D systems.

Keywords:Anderson Localization of light; dimensionless conductance; polarization coupling terms

Summary

1 Introduction

The work developed by P. W. Anderson [1] investigates the transport properties of electrons in disordered materials. He demonstrates that, provided the potential associated with the surrounding nuclei is sufficiently disordered, electrons become localized, meaning that its probability density is confined to a small region of space. Furthermore, in this regime the spatial decay of the electron wave function is exponential. Due to these localized electronic wave functions, the material transitions from a conductor to an insulator, resulting in significantly reduced transport [2].

To determine whether the disordered material is in the localized regime, one can measure the electrical conductance. This conductance depends on the material length, similar to how resistance depends on the wire size, as described by Ohm's law. If the conductance is much greater than 1, the material is conductive, implying that the eletronic wavefunctions are extended throughout the disordered material. Conversely, when the conductance is much smaller than 1, the electron remains confined to a limited region of space. This localization phenomenon induces a transition to an insulating phase in the material. In the context of Anderson localization and the scaling theory (which will be discussed later), this conductance is referred to as the Thouless number.

The dimensionless conductance g accounts for how dimensionality (that is, 1D, 2D, or 3D systems) affects the localization transition (or its absence). For 1D and 2D systems, according to the scaling theory [3] the conductance is always less than 1, indicating that, regardless of the system size, there will always be localized modes. In contrast, for a 3D system, if the conductance exceeds 1 (conductor), increasing the system size will result in a higher value of g. However, if the conductance is less than 1 (insulator), which typically occurs in the strong-disorder limit, g will decay exponentially. In this context, the scaling theory was proposed, which assumes that the conductance curve displays a transition from the extended to the localized regime. In particular, this critical point can be determined through the scaling of the conductance with the system size.

Although the work developed by P. W. Anderson and his collaborators [4, 5] focused on electron localization, the phenomenon was later shown to be inherently tied to the wave nature of electrons and applies to other types of waves. Consequently, both the dimensionless conductance and the scaling theory should also hold for various types of waves. Despite the consistency of Anderson's model, using electrons to describe the metal-insulator transition presents experimental and analytical challenges. This is because electrons strongly interact with one another, whereas the proposed theory is a single-particle model that assumes no interactions. Recognizing that the experimental observation

of Anderson localization for electrons would be challenging, given its original formulation for non-interacting electrons, a decline in studies dedicated to this system was observed [6].

Later, new works [5] proposed using light to investigate localization. Unlike electrons, photons are non-interacting particles, which facilitates the setup of experiments to verify light localization in disordered media [7, 8, 9]. Nevertheless, even in the context of single photons, the localization of light in 3D atomic systems remains a topic of debate within the scientific community [10, 11]. To better understand the underlying problems, 1D and 2D configurations have been studied as well [12, 13, 14]. The primary reason for the absence of localization of 3D disordered systems is the polarization property of light, which transfers momentum to atoms, and generate near-field interactions between scatterers.

As demonstrated in previous [12], considering a 2D model leads to decoupling into two independent scattering channels. The first is the scalar channel, where the interaction terms are uniform when considering light with linear polarization, meaning polarization can be disregarded. In the vectorial channel, near-field interaction terms inhibit localization. This is at odds from the scaling theory which predicts that all 2D systems localize, in the large size limit. Then, considering that near-field terms become negligible in the dilute limit, one may question whether localization is restored in 2D dilute systems. This Master dissertation addresses this point, aiming at the study of Anderson localization in a 2D disordered atomic cloud within the vectorial channel for a large number of particles, ensuring that the cloud's radius is sufficiently large for near-field terms to become negligible.

In the first chapter, we provide a theoretical introduction to wave scattering in disordered media, explaining the phenomenon preceding Anderson localization, known as weak localization. Subsequently, we offer a brief introduction to the concepts of Anderson localization, dimensionless conductance, and scaling theory. We conclude this chapter with an introduction to the phenomenon of light localization, including examples and a concise explanation of the theory underlying the two-dimensional model. In the second chapter, we describe the model used in this study, along with the mathematical tools employed to identify localized modes, such as the decay rate, the mode's center of mass, and the localization length. We then calculate parameters for different atomic clouds with the same density regime to examine how these tools aid in studying localized modes in different channels. Additionally, we perform calculations for atomic clouds in the low-density regime to achieve the largest possible atomic radius, focusing primarily on analyzing the ratio between the localization length and the system radius. This chapter concludes with the calculation of the conductance g for various density regimes and channels, enabling predictions of the number of atoms required to potentially observe localized modes in the vectorial channel. Finally, we present the conclusion, revisiting the key concepts discussed throughout the work, analyzing the results in greater depth, and proposing future steps to investigate the observation of localized modes in the vectorial channel.

2 Theoretical Foundation

Matter may scatter the light through different processes.For example, light can be either scattered inelastically, which alters its frequency, or elastically, preserving its spectral features. The structure of the scattering medium also plays a crucial role especially whether it is ordered or disordered. In this dissertation, we focus on elastic scattering the effects in fully disordered media. This situation is particularly complex , yet it is present in everyday life, such as in clouds, white paint, and milk.

Wave propagation in disordered media typically depends on physical characteristics, such as the sample size L, the wavelength λ, and the mean free path ℓ. This typical distance between two scattering events represents the relevant length scale to distinguish different scattering regimes. When the sample size is much smaller than the mean free path ($L \ll \ell$), single scattering dominates. In other words, the wave typically undergoes less than one scattering event before exiting the disordered medium. Another regime of interest is the ballistic one, when the sample size is much larger than the mean free path ($L \gg \ell$), multiple scattering then dominates, and the light wave typically experiences many scattering events. I.e. the wave experiences more than one scattering event before leaving the sample. Within this multiple scattering regime two distinct categories of wave transport can be distinguished [15].

The first category is diffusive transport, where the mean free path is much larger than the wavelength ($\ell \gg \lambda$). In this case, the interference of multiple scattered waves is negligible and two scattering events are typically separated by a distance ℓ. Wave transport in a random medium under this condition is described by the diffusion equation, and the medium is referred to as a weakly disordered medium. The second category arises when the disorder is increased to the extent that the mean free path becomes comparable to or smaller than the wavelength ($\ell \lesssim \lambda$). This may lead to the localized regime, where the medium is strongly disordered yet diffusive wave transport no longer occurs. This phenomenon, involving wave interference, is known as Anderson localization [1].

In this chapter, we provide a brief description of diffusive transport in weakly disordered media. In this regime, we observe the effect of coherent backscattering, also known as weak localization. Subsequently, we introduce Anderson localization, expanding on the interpretation of the localized regime and discussing the dependence of sample size on Anderson localization. Following this, we present the scaling theory, which provides a foundation for understanding what occurs in a localized regime as the system size increases. This includes the Thouless number, derived from the electron localization model, which describes a measurable property that indicates whether a system is localized or not. Finally,

we introduce Anderson localization of light, addressing the key differences with the electron localization model and emphasizing the still unobserved Anderson localization of light in three-dimensional (3D) systems.

2.1 Diffusive Transport

When a wave propagates through a medium containing multiple scatterers, we encounter diffusive transport, as previously discussed. In our daily experience, an example of this phenomenon is heat conduction. While this provides a clear example, diffusive transport of waves raises important questions about fundamental principles, particularly in the context of quasi-quantum behavior. The description of the diffusion of multiply scattered waves cannot be entirely accurate. For causality dictates that information has a finite speed. Therefore, no signal or disturbance can propagate instantaneously. But in diffusion-based models, the disturbance can propagate instantaneously throughout the material. And waves not only carry energy, they also carry phase information, which describes phenomena such as interference and coherence. Regardless of its appearance, a multiply scattered wave remains a solution to the wave equation (albeit with random coefficients) and, as such, must satisfy the fundamental properties of its solution [15].

Furthermore, wave diffusion must exhibit some deviation from classical diffusion, where the wave nature should have a more significant influence. Therefore, in this section, we discuss how, starting from diffusive transport, we can arrive at coherent backscattering, which is typically considered a precursor to Anderson localization in weakly disordered media.

In Fig.1, two rays propagate through a weakly disordered medium, both with the same frequency. The wave propagation from point $\mathbf{r}$ to point $\mathbf{r}'$ can occur along infinitely many different paths. The path of ray A has an amplitude A_I at a distant source point $\mathbf{R}_0$ and wave vector $\mathbf{k}_I$. After n scattering events, the path of ray A exits the front surface with wave vector $\mathbf{k}_F$. The spatial locations of the n scatterers are consecutively labeled as $r = r_1, r_2, r_3, \ldots, r_n = r'$. Since all scatterings are elastic, the complex amplitude A_0 of the path of ray A at a distant observation point $\mathbf{R}_0$ can be related to A_I as:

$$A_0 = A_I G_A \exp\left[i\mathbf{k}_I(\mathbf{r}_1-\mathbf{R}_0)+i\mathbf{k}_{1,2}(\mathbf{r}_2-\mathbf{r}_1)+\cdots+i\mathbf{k}_{n-1,n}(\mathbf{r}_n-\mathbf{r}_{n-1})+i\mathbf{k}_F(\mathbf{r}_0-\mathbf{r}_n)\right]. \quad (2.1)$$

Here $\mathbf{k}_{n-1,n}$ is the wave vector of the ray propagation between scatterers $n-1$ and n, and G_A is a factor that accounts for the scattering strength of each scatterer. Simplifying the notation: $A_0 = A_I G_A \exp[i\phi_A]$.

For each diffusive path A, consisting of n scatterers such that the wave is scattered by these scatterers in the order $1 \to 2 \to \ldots \to n$, there exists a time-reversed counterpart

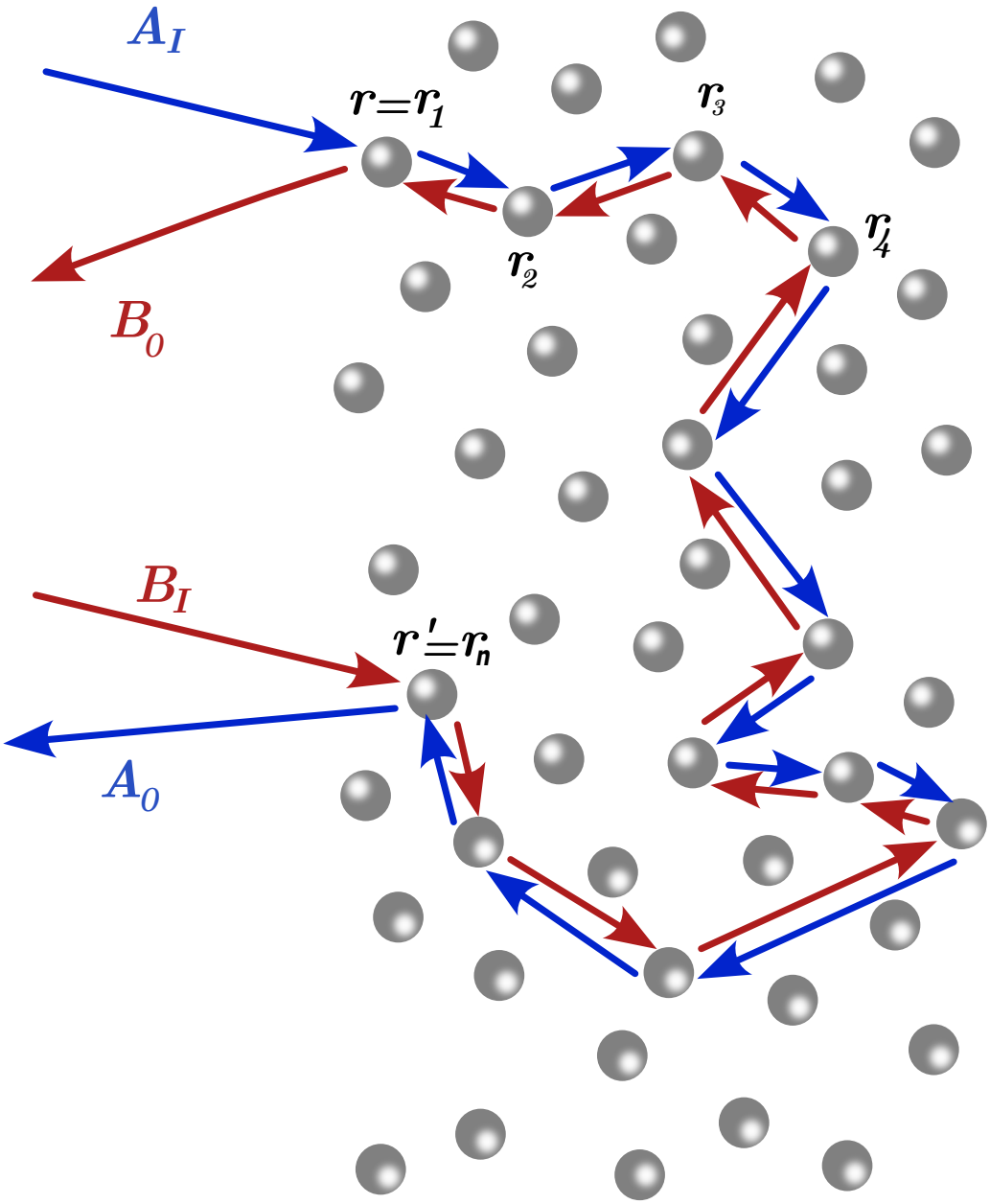

Figure 1 – A schematic illustration of two interfering rays, A and B. Ray B's path is scattered through $r = r_1, r_2, \ldots, r_n = r'$, while ray A's path follows precisely the opposite scattering order. This arrangement is intentional, because ray B's path can then be regarded as ray A's path propagating backward in time between $\mathbf{r}_1$ and $\mathbf{r}_n$.

B, which consists of the same n scatterers but with propagation in the reverse order $n \to \ldots \to 2 \to 1$. In other words, the path of ray B starts at $\mathbf{r}' = \mathbf{r}_n$ and ends at $\mathbf{r} = \mathbf{r}_1$. The reversed path B can be viewed as the direct path A propagating backward in time, hence the term "time-reversed paths". The path of ray B has amplitude $B_I = A_I$ at the same source point $\mathbf{R}_0$ and the same incident and exit wave vectors $\mathbf{k}_I$ and $\mathbf{k}_F$ as A. Similarly, for path B, the amplitude B_0 at the same distant observation point $\mathbf{r}_0$ can be

related as:

$$B_0 = B_I G_B \exp\Big[i\mathbf{k}_I(\mathbf{r}_n - \mathbf{R}_0) + i\mathbf{k}_{n,n-1}(\mathbf{r}_{n-1} - \mathbf{r}_n) + \cdots + i\mathbf{k}_{2,1}(\mathbf{r}_1 - \mathbf{r}_2) + i\mathbf{k}_F(\mathbf{r}_o - \mathbf{r}_1)\Big], \quad (2.2)$$

where G_B is a factor similar to G_A. This can also be simplified as $B_0 = B_I G_B \exp[i\phi_B]$. Since identical scattering events are involved, $G_A = G_B$.

Now we are interested in calculating the probability that the diffuse-path rays A and B travel from $\mathbf{r}_1$ to $\mathbf{r}_n$:

$$P = |A_0 + B_0|^2 = |A_0|^2 + |B_0|^2 + A_0 B_0^* + A_0^* B_0, \quad (2.3)$$

where the complex conjugate amplitude values for each path can be written as $A_0^* = A_I G_A \exp[-i\phi_A]$ and $B_0^* = B_I G_B \exp[-i\phi_B]$. Furthermore, we know that $|A_0|^2 = |B_0|^2 = |A_I G_A|^2$. Thus, we can calculate the last two terms of Equation 2.3 as follows:

$$A_0 B_0^* = |A_0|^2 \exp[i\phi_A - i\phi_B] = |A_0|^2 \exp[i\Delta\phi], \quad (2.4)$$

and

$$A_0^* B_0 = |A_0|^2 \exp[-i\phi_A + i\phi_B] = |A_0|^2 \exp[-i\Delta\phi], \quad (2.5)$$

where $\Delta\phi = [\phi_A - \phi_B]$. Because these paths are time-reversed, we have $\mathbf{k}_{n,n-1} = -\mathbf{k}_{n-1,n}$. Thus, we can simplify the phase difference to $\Delta\phi = (\mathbf{k}_I + \mathbf{k}_F) \cdot (\mathbf{r}_1 - \mathbf{r}_n)$. Finally, we can rewrite the probability that the diffuse-path rays A and B travel from $\mathbf{r}_1$ to $\mathbf{r}_n$ as follows:

$$P = |A_0|^2 + |A_0|^2 + |A_0|^2 \exp[i\Delta\phi] + |A_0|^2 \exp[-i\Delta\phi]. \quad (2.6)$$

Using Euler's relation, which states that $\exp[i\theta] + \exp[-i\theta] = 2\cos[\theta]$, we obtain:

$$\begin{aligned} P &= 2|A_0|^2\{1 + \cos[\Delta\phi]\} \\ &= 2|A_0|^2\Big\{1 + \cos[(\mathbf{k}_i + \mathbf{k}_f) \cdot (\mathbf{r} - \mathbf{r}')]\Big\}. \end{aligned} \quad (2.7)$$

In Equation 2.7, inside the braces, the constant term (1) appears due to incoherent scattering, $2|A_0|^2$, and the term $\cos[(\mathbf{k}_i + \mathbf{k}_f) \cdot (\mathbf{r} - \mathbf{r}')]$ arises from the interference terms $A_0 B_0^* + A_0^* B_0$. We define the incoherent term to mean waves with different propagation directions but the same frequency. When we consider the elastic scattering of particles, we disregard the interference term. However, when we study the quantum model, the wave properties are reinforced, causing the interference terms to have a strong influence on the scattering [16].

This case occurs when $\Delta\Phi = 0$, so the time-reversed paths are perfectly coherent. This happens in two different ways: when $\mathbf{k}_F = -\mathbf{k}_I$, indicating that the two outgoing rays are exactly coherent in the direction opposite to the incident direction, or when the multiply scattered wave returns to the initial scattering center, $\mathbf{r}_1 = \mathbf{r}_N$, forming a closed loop. The first corresponds to incoming and outgoing waves, meaning that the wave

incident on the medium is then multiply scattered in the backward direction, which is relevant to the phenomenon of coherent backscattering.

The coherent backscattering effect takes its name from the following effect: after a wave is multiply scattered many times, some coherence is preserved in the direction opposite to its incident direction (the backscattering direction) but not in other directions. By preserving coherence in the backscattering direction, the probability of backscattering is enhanced through constructive interference. In this case, the closer $\mathbf{k}_f$ is to $-\mathbf{k}_i$ for fixed $\mathbf{r}$ and $\mathbf{r}'$, the greater the probability. At the maximum value, where $\mathbf{k}_i + \mathbf{k}_f = 0$, coherence increases the backscattering intensity, resulting in $P = 4|A_0|^2$.

In the second case, recurrent scattering occurs within a medium, without coupling to the external world. In other words, closed paths (loops) form, and the initial point $\mathbf{r}_1$ and the final point $\mathbf{r}_n$ coincide ($\mathbf{r}_1 = \mathbf{r}_n$). Therefore, time-reversed loops interfere constructively. Hence, in the scenario where $\mathbf{r}_1$ and $\mathbf{r}_n$ are identical, it represents the probability that the wave is scattered back to the scattering center from which it originated, that is, the return probability to the initial point $\mathbf{r}_1$, which is also $P = 4|A_0|^2$. Thus, by preserving coherence in the backscattering direction (the return to the point of origin), the probability of backscattering is enhanced through constructive interference. The probability of propagating away from the origin (incoherent wave propagation) is $2|A_0|^2$, meaning that the probability of diffusive wave transport through the sample is lower than the probability of being trapped. In the electron transport model, interference effects in the weak-disorder limit reduce the diffusion coefficient and, therefore, the conductivity. This effect, which manifests as a decrease in the diffusion coefficient under weak disorder, is called weak localization and is considered a precursor to the strong (Anderson) localization effect. In the literature, the latter is sometimes presented as a consequence of coherent backscattering [15].

As already mentioned, these effects occur in a weakly disordered medium. Now, let us analyze the system in a strongly disordered medium. Starting from the diffusion coefficient according to kinetic theory, which is expressed as $D = \frac{1}{3}v\ell$, where v is the velocity of the particle or wave that is scattering, and ℓ is the mean free path. As the disorder increases, the probability of forming time-reversed loops also increases because the distance between scatterers is reduced. This higher density of time-reversed loops leads to constructive interference in the transmitted intensity. In other words, when the probability of forming time-reversed loops is greater than the probability of diffusive paths, the diffusion coefficient becomes zero and the wave becomes trapped, i.e., localized within the medium. Thus, above a critical level of disorder, the number of time-reversed loops diverges, leading to the transition to strong (Anderson) localization [17].

The phase transition from the diffusive regime to the localized regime is a feature unique to a 3D disordered medium. In 1D and 2D disordered media, the diffusive particle

repeatedly returns to the point of origin, making the probability of time-inverted closed loops extremely high. Consequently, at low dimensionalities (1D and 2D), waves can be localized even for very weak disorder. This does not occur in 3D because diffusive wave propagation in a 3D disordered medium is not recurrent. Thus, under weak disorder, the probability of having closed loops is lower than in lower dimensions. When considering the wavelike nature of particles, there is a deviation from classical diffusion, allowing us to explain coherent backscattering (weak disorder) and Anderson localization (strong disorder). The coherent backscattering effect is valid only when the system is time-reversal invariant, meaning that no macroscopic preferred time direction is established. Examples of breaking of this invariance are the uniform average velocity of the scatterers or the presence of a magnetic field. Then the correction to the wave diffusion constant is reduced. Therefore, explaining the occurrence of Anderson localization based on closed time-reversed loops and constructive interference only provides an estimate of the lowest-order correction (weak localization) to the diffusion constant [15].

In the following section, we introduce Anderson localization, providing a brief explanation of the adopted model, along with some examples of localization for different types of waves.

2.2 Introduction to Anderson Localization

The classical Drude conductance theory (1900) was based on the idea that free electrons are scattered by positive ions in a periodic lattice. An important part of this theory is the description of the mean free path ℓ, which is the average distance that electrons travel before colliding with an ion in the lattice. With the formation of energy bands, it became possible to explain electrically conductive and insulating materials. Thus, the conductance of a material or atomic lattice is related to the average time between these collisions.

With the discovery of quantum mechanics, it was understood that an electron in a material diffracts in an ideal crystal, behaving like a wave. In this context, the concept of electrical resistance can be defined when electrons are scattered by crystal imperfections. With the revision of quantum mechanics, the Drude model can still be used, but it considers the electron moving in a zigzag path among impurities. Therefore, the greater the number of impurities in the material, the shorter the mean free path will be and, consequently, the lower the material's conductance [6].

The work developed by P. W. Anderson [1] to describe the metal-insulator transition went beyond its initial scope. Indeed, in certain materials, if electrons are considered non-interacting quantum particles, they exhibit wavelike phenomena. Anderson's proposed

model is a tight-binding approach with an electron that can hop between nearest neighbors in a 3D lattice with disorder. The system was represented as a three-dimensional lattice with random energies. This model depicted two regimes: the first diffusive regime, in which states extend throughout the disordered medium, making the material conductive (metallic). In this regime, these electrons can be transported across the entire material.

In the second regime, the localized regime, there is no diffusive transport. Because only localized states are present, the material is thus insulating. Moreover, these states are exponentially localized, so the electron's wavefunction decays starting from r_0. Hence:

$$|\psi(r)|^2 \propto \exp\Big(|r - r_0|/\xi\Big), \tag{2.8}$$

where ξ is the localization length [6]. In Figure 2(a), we see a nearly perfect crystalline lattice with a mean free path ℓ and the electron's Bloch function in an extended state, meaning that the wavefunction is distributed throughout the crystalline lattice. By contrast, Figure 2(b) shows a disordered crystalline lattice and the electron's Bloch function in a localized state, exhibiting an exponential decay in space [2].

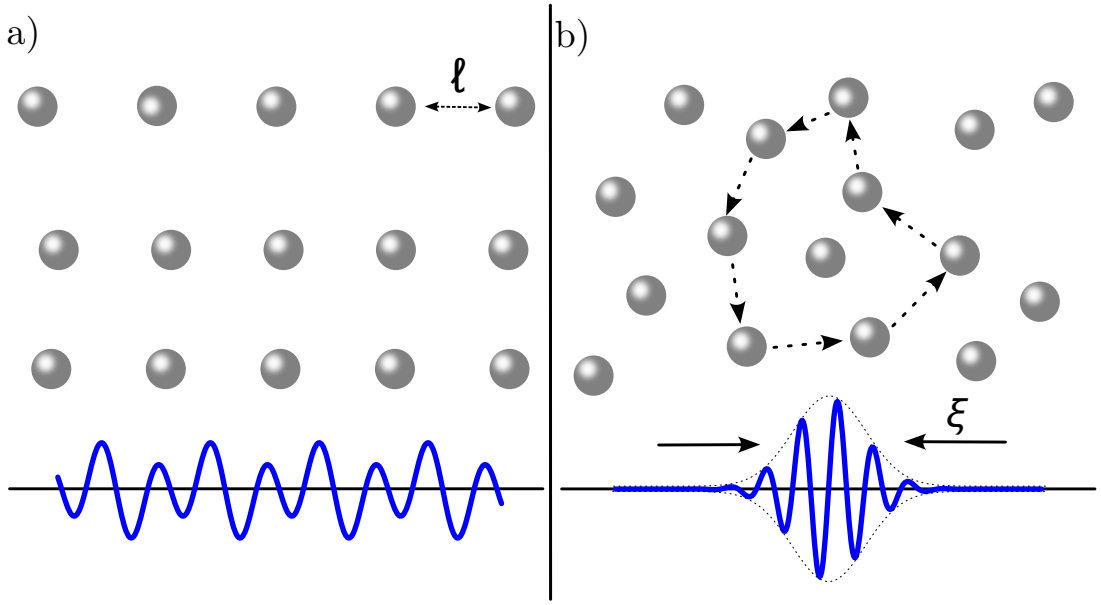

Figure 2 – a) Bloch function in a nearly perfect crystal with an extended state and mean free path ℓ. b) Interference effects on wave propagation in a disordered lattice, a localized state with the localization length ξ.

An important step in the understanding of the localization phenomenon was achieved through the scaling theory of localization [3], which was addressed in the following section. Anderson localization, often called strong localization, is the spatial localization caused by disorder (impurities, random positions of scattering centers, etc.). It is a physical phenomenon that has been experimentally observed for different types of waves, and its underlying concepts have been investigated in various analytical contexts. However, Anderson localization for light in 3D has not yet been experimentally observed. Translucent

objects such as bones, marine corals, and marble are naturally disordered, but their disorder levels are small compared to the amount required to localize light. Nonetheless, it is possible to fabricate materials with higher degrees of disorder. For example, titania powder [7] has a high refractive index, submicron grain size, and a mean free path on the order of the wavelength.

The challenge of localizing light lies in finding a material that can maximize scattering without absorption. Indeed, absorption will provide an exponential decay of the propagating wave without localization being involved. One solution was to use a light frequency lower than the bandgap of a semiconductor, thereby avoiding absorption, and to ensure that this semiconductor has a high refractive index. Gallium arsenide powder was used, and what was initially interpreted as nearly complete localization of infrared light was observed [8].

Finally, when atoms are at temperatures close to absolute zero, their de Broglie wavelengths are on the order of 10^{-6} m, so they behave like waves. It has been observed that the expansion of ultracold atoms in a 1D disordered potential can be halted. The studied system is an optical interference pattern that generates a random potential from which the atoms scatter. The advantage of cold atoms over electrons is the ability to tune the interactions [18].

2.3 Dimensionless conductance

The scaling theory aims to describe the emergence of extended wave states and localized wave states as independently as possible from the physical model's details. For example, a theory that describes localization regardless of the type of lattice—whether simple cubic, body-centered cubic, or any other geometry. In this sense, the scaling theory implies broad applicability, seeking a model of the phenomenon without being overburdened by details. It relies primarily on the change in the transport properties when increasing the scale, or physical size, of the sample under consideration. More specifically, the scaling theory of localization focuses on how a quantity, defined as the dimensionless conductance g, varies with a change in the sample size.

Let us, first consider a material divided into many smaller cubes of various sizes L. Since these cubes are three-dimensional, we consider $d = 3$ yet the theory generalizes to any dimension. By introducing a single-frequency source of excitation at the center of each cube, one can detect the response on the faces of these cubes. Depending on the situation inside a given cube, there may be a localized or an extended state. For the localized state, we assume the sample size is larger than the confinement length of that mode ($L > \xi$). It is possible to distinguish these states by increasing the sample size L. The response of a

localized state decreases exponentially as the sample size increases. Conversely, for the extended case, the surface response of the sample remains constant. Since the localized mode tends to zero as the sample size surpasses the localization length, it differs from the extended mode [19].

To quantify this approach, the argument above must focus on how the wavefunction responds when the boundary conditions on the surfaces are changed. In this case, the response is a frequency shift $\delta\omega$, defined as the difference in eigenvalues when the boundary condition changes. An example would be a vibrating string: when its length changes, the frequency also changes.

If the sample is homogeneous, this change in boundary condition is equivalent to adding or subtracting an extra half-wave, resulting in a wavevector shift by $\delta k = \pi/L$. For the electronic case, $\omega = \hbar k^2/2m$, so

$$\delta\omega = \left(\frac{\hbar}{m}\right)\delta k = \frac{v\pi}{L}, \tag{2.9}$$

where $\hbar$ is Planck's constant and m is the electron mass. For a classical scalar wave, $\omega = v_0 k$, then

$$\delta\omega = \frac{v_0\pi}{L}, \tag{2.10}$$

where v_0 is the scalar wave velocity. In both cases, $\delta\omega$ is inversely proportional to a certain timescale: the time the wave needs to travel from one end of the sample to the other, which is related to the diffusion time.

However, if the sample is inhomogeneous, calculating $\delta\omega$ is not trivial. A discussion will follow. Nevertheless, as in the homogeneous case, $\delta\omega$ is proportional to the diffusion time. Thus, the time required for a particle to diffuse across the block is

$$\tau(L) = \frac{L^2}{D}, \tag{2.11}$$

where D is the diffusion constant. Using the uncertainty principle, we find

$$\delta\omega = \frac{\hbar D}{L^2}. \tag{2.12}$$

Hence, if the signal propagation is diffusive in a non-homogeneous medium, the dependence on L^2 remains. In contrast, exponentially localized states are not affected by changes in the boundary conditions. Therefore, the frequency difference for different L values must be exponentially small. For $L \gg \xi$,

$$\delta\omega \propto \exp(-L/\xi), \tag{2.13}$$

and so, the larger L becomes, the closer $\delta\omega$ is to zero. This frequency difference alone does not help categorize whether the modes are more localized or more extended; one needs a

reference "typical size" for comparison. Thouless used the average energy-level spacing inside the block, which can be represented as

$$\Delta\omega = \left(n_E L^d\right)^{-1}, \tag{2.14}$$

where n_E is the density of states (i.e., the number of states per unit volume per unit energy) and d is the dimension ($d = 3$ in our case). This average energy-level spacing is useful to compare how large $\delta\omega$ becomes [15].

For small L, few modes fit in the sample, so the energy-level spacing is large. When L is large, there are many modes that can occupy the cube, and thus the energy-level spacing is small. An analogy is to imagine a small ukulele (L small), which has space for fewer notes, so the difference between them is bigger when compared to a guitar (L large). A guitar has more possible notes, so the spacing between them is smaller.

Hence, as a quantitative measure of sensitivity to a change in boundary conditions, the frequency shift $\delta\omega$ must be compared to the average frequency separation $\Delta\omega$ between neighboring eigenvalues. The dimensionless ratio $\delta\omega/\Delta\omega$ is denoted

$$g = \frac{\delta\omega}{\Delta\omega}. \tag{2.15}$$

Now, let us analyze what happens to g in each regime. For both the localized and the diffusive regime, $\Delta\omega \propto L^{-d}$. In the extended case, $\delta\omega \propto L^{-2}$. Therefore, in a 3D system, g is proportional to L, i.e., $g \propto L^{d-2}$ in general. For localized states, $\delta\omega$ decays exponentially with L for L beyond ξ. Thus, g always decreases exponentially as L increases for localized states [16].

A way to analyze g in relation to sample size is to combine smaller samples to form larger samples, still considering the case $d = 3$. Thus, if the frequency difference $\delta\omega$ is much greater than the average frequency separation $\Delta\omega$, the cube's eigenstates can overlap among all cubes, ensuring the formation of new extended states. For larger samples, that is, by increasing L, $\delta\omega$ decreases proportionally to L^2, while $\Delta\omega$ decreases proportionally to L^3. Thus, for extended states, we maintain $\delta\omega \gg \Delta\omega$.

However, if the average frequency separation $\Delta\omega$ is much smaller than the frequency difference $\delta\omega$, the eigenstates will have difficulty overlapping among all cubes, and the states remain localized. In this scenario, for larger samples (by increasing L), $\delta\omega$ decays exponentially, whereas $\Delta\omega$ decays with L^3. Consequently, in the localized state, $\delta\omega \ll \Delta\omega$ holds for any size of L.

Therefore, in a three-dimensional system, one can use $g(L)$ to distinguish between extended and localized states. If $g(L) \gg 1$, the system has extended states, whereas if $g(L) \ll 1$, it has localized states. Hence, we can imagine that there exists a value $g = g_c$ at which the behavior crosses over from extended states to localized states. Furthermore,

the transition from the extended regime to the localized regime is expected to occur when $\Delta\omega$ and $\delta\omega$ are of the same order of magnitude, that is, when $g_c(L) \sim 1$. This plausible assumption of a critical g_c is an essential element of the scaling theory of localization.

Knowing that $g \propto L^{d-2}$ in an extended regime, we consider the case $d = 1$. As the sample size increases, g decreases at a rate of $1/L$, so it never exceeds $g_c(L) \sim 1$. Therefore, in one-dimensional random systems, only localized states can exist. For the case of $d = 2$, the ratio $\delta\omega/\Delta\omega$ remains constant in the "extended state" limit, so it can proceed in any direction. Consequently, the scaling argument indicates that the localization phenomenon is sensitive to the sample's spatial dimensionality, with $d = 2$ as the critical dimension for localization.

Let us apply the concept of conductance to an electronic system, because the quantity g can be interpreted as the electrical conductance. In an electronic system, g is simply the conductance G divided by the quantum unit of conductance, e^2/h, where e denotes the electronic charge and h is Planck's constant. From Einstein's relation and from the fact that $G_E = \sigma_E L^{d-2}$, it follows that:

$$G_E = \frac{e^2}{\hbar} D\rho_e(\omega) L^{d-2}. \tag{2.16}$$

Using Thouless's argument that $\delta\omega L^2 = D$, where $\delta\omega = \Delta\omega/2\pi$, we obtain:

$$G_E = \frac{e^2}{\hbar}\frac{\delta\omega}{2\pi} L^2 \frac{1}{\delta\omega L^d} L^{d-2} = \frac{e^2}{\hbar} g, \tag{2.17}$$

where $g = \delta\omega/\Delta\omega$. Thus, for electrons in a weakly disordered medium, we use equations 2.14 and 2.12 and conclude that $g(L) \propto L^{d-2}$. In the localized regime, using equations 2.14 and 2.13, we find that $g(L) \propto \exp(-2L/\xi)$ for $L \gg \xi$. We therefore reach the same conclusions as in the general case [19].

In the next section, we discuss the approach which connects extended and localized states without requiring the system size to be known. Using this theory, it is possible categorize the conducting/isolating regime solely by the dimensionless conductance value.

2.4 Single-Parameter Scaling Theory

Thouless and collaborators' work led to the conclusion that conductance is the parameter that controls the system's behavior. In addition, we know that the transition from the diffusive regime to the localized regime must be continuous [20]. Based on these ideas, in 1979, the "Gang of Four" (E. Abrahams, P. W. Anderson, D. C. Licciardello, and T. V. Ramakrishnan) formulated the scaling theory of localization [3], a phenomenological theory that connects extended and localized states.

As an illustrative example of this behavior, consider a bar of size (L) that has the same disorder properties along its length, with conductance $g(L)$. If we increase this bar by a distance (bL), and because the conductance depends only on this bar, the new conductance must be a function of $g(L)$ and the ratio by which the bar was extended. We can then write the new conductance as $g(L + bL) = f(b, g(L))$. Because we want the variation in conductance, Δg, to be proportional to this increase, we can write:

$$\frac{g(L + bL) - g(L)}{bL} = \frac{f(b, g(L)) - g(L)}{bL} \tag{2.18}$$

In the literature, the parameter $\beta(g)$ describes how the conductance changes. The scaling function $\beta(g)$ is given by:

$$\beta(g) = \lim_{b \to 0} \frac{f(b, g(L)) - g(L)}{g\, L}, \tag{2.19}$$

so we can rewrite Equation 2.18 using 2.19 as:

$$\lim_{b \to 0} \frac{g(L + bL) - g(L)}{bL} = \frac{g(L)}{L}\, \beta(g), \tag{2.20}$$

$$\lim_{b \to 0} \frac{g(L + bL) - g(L)}{bL} = \frac{g(L)\, \beta(g)}{L}. \tag{2.21}$$

We know that:

$$\lim_{b \to 0} \frac{g(L + bL) - g(L)}{bL} = \frac{d\, g(L)}{dL}.$$

Therefore,

$$\frac{d\,[g(L)]}{dL} = \frac{g(L)\, \beta(g)}{L},$$

$$\beta(g) = \frac{d\,[g(L)]}{dL}\, \frac{L}{g(L)}. \tag{2.22}$$

Since

$$\frac{d\,[\ln\, g(L)]}{d\, \ln\, L} = \frac{d\,[g(L)]}{dL}\, \frac{L}{g(L)},$$

we conclude that Equation 2.22 can be written as:

$$\beta(g) = \frac{d\, \ln\, g(L)}{d\, \ln\, L}. \tag{2.23}$$

As previously discussed, there are two different behaviors for the conductance $g(L)$, depending on whether the state is extended or localized. Before analyzing how $\beta(g)$ varies for each regime, we can extract information by examining $\ln g(L)$:

$$\ln g(L) \propto \begin{cases} (d-2) \ln L & \text{for the extended state} \\ -\exp(\ln L) & \text{for the localized state.} \end{cases}$$

For an extended state in 3D, as L increases, $\ln g$ also increases. Conversely, for a localized state, $\ln g$ always decreases exponentially. In 1D and 2D, as previously discussed, the system is always in a localized state.

We can now analyze how $\beta(g)$ varies in each regime.

$$\beta(g) \propto \begin{cases} d-2-\frac{a}{g} & \text{for the extended state} \\ \ln(g) & \text{for the localized state.} \end{cases}$$

In localized states, this derivative is negative, which differs from the 3D case in the diffusive regime. Therefore, when $\beta(g) > 0$, the states are extended, a phenomenon that occurs only in 3D systems. However, when $\beta(g) < 0$, it indicates that the states are localized. In a three-dimensional system, there is a critical transition conductance g_c, which occurs when $\beta = 0$. In the case of weak disorder, $g(L) > g_c$, and thus $\beta(g) > 0$ [15].

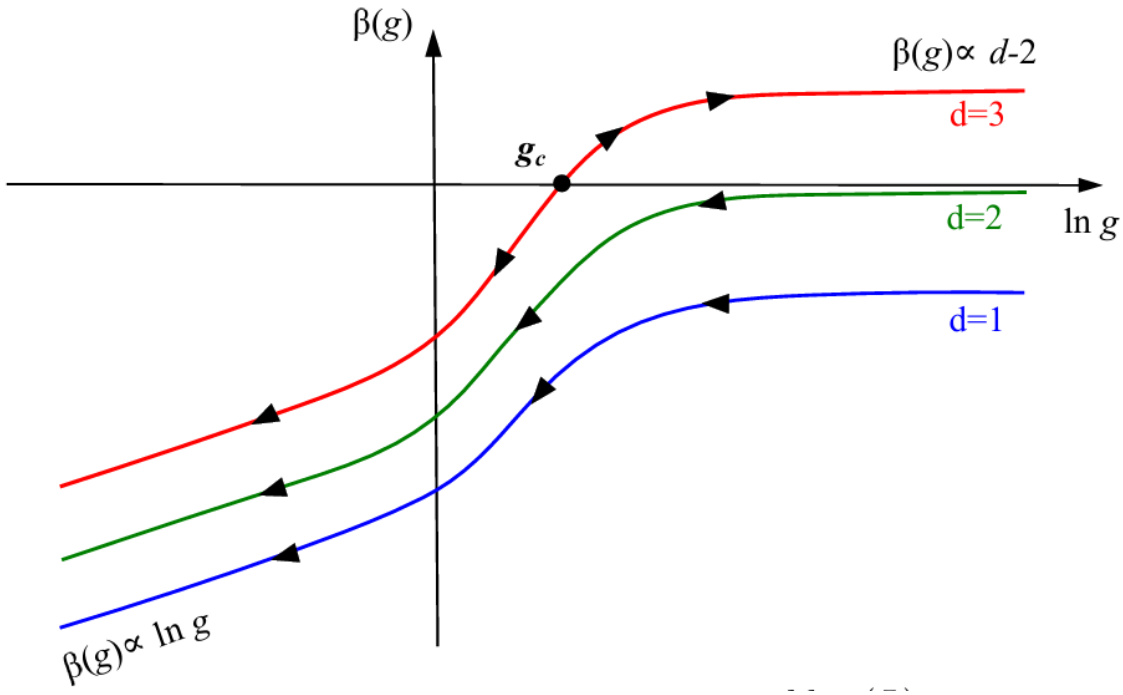

Figure 3 – A schematic image showing the behavior of the scaling function. The image is constructed from the known asymptotic behavior of $\beta(\ln g)$ in different spatial dimensions, along with the assumption of continuity. The arrows indicate the directions of variation as the sample size L increases.

Assuming that $\beta(g)$ is a continuous function, Figure 3 shows a sketch of the $\beta(g)$ curve for dimensions $d = 1, 2, 3$. The arrows on each curve depict how g changes as L increases. As previously discussed based on the equations, the behavior of $\beta(g)$ strongly depends on the dimensionality of the system. The figure shows that for $d = 1$ and $d = 2$, $\beta(g)$ is always negative. Hence, when the system size increases, the conductance always converges to its localized-regime limit. Therefore, for $d \leq 2$, the system inevitably reaches the localized regime, regardless of the degree of disorder, provided that the length scale is sufficiently large ($L \gg \xi$).

In the case of $d = 3$, there is a critical point $g_c \sim 1$, given by $\beta(g_c) = 0$, where $\beta(g)$ changes sign. This critical point $\big(\beta(g_c) = 0\big)$ separates the two regimes and corresponds

to the Anderson transition between the extended regime and the localized regime. We thus conclude that scaling theory not only predicts the existence of a transition from the extended regime to the localized regime in 3D but also indicates that all modes in 1D and 2D systems in disordered media are localized.

In the following section, we introduce Anderson localization for light, since all the effects discussed in this section occur due to wave-like behavior. We also highlight why light localization offers certain advantages when compared to electron localization.

2.5 Anderson localization of light

Anderson localization, originally proposed by P. W. Anderson in the context of electrons in disordered materials, has become a powerful tool for understanding transport phenomena in disordered systems. Initially limited to quantum systems, its application was extended to classical waves around 1980, allowing the study of localization in electromagnetic, acoustic, and elastic waves [18].

In the specific case of light, the study of localization has received increasing attention due to the peculiar characteristics of photons. Unlike electrons, photons do not directly interact with each other, which allows researchers to investigate their transport phenomena under conditions in which interactions do not mask disorder effects. Moreover, photons have a significantly longer coherence length than electrons, making localization experimentally verifiable at room temperature and in macroscopic samples.

To discuss and draw an analogy between light localization and electron localization, we use the wave equation for an electron with reduced mass m in a disordered lattice:

$$-\left[\frac{\hbar^2}{2m}\nabla^2 + \widetilde{V_r}(x)\right]\psi(x) = E\psi(x). \tag{2.24}$$

The random potential $\widetilde{V_r}(x)$ experienced by the electron results from the presence of impurities or defects in the material's crystalline lattice. To confine this electron, the energy E must be much lower than $\widetilde{V_r}(x)$ because the probability of finding the electron outside the potential increases with higher energy E. For $E < \widetilde{V_r}(x)$, the electron has the probability of tunneling through the potential [21].

For a monochromatic electromagnetic wave of frequency ω propagating in a random medium with a heterogeneous dielectric, whose dielectric constant is positive and can be written as $\epsilon(x) = \bar{\epsilon} + \delta\epsilon$, the disorder in the medium comes from the variation of the term $\delta\epsilon$, and $\bar{\epsilon}$ is the average of $\epsilon(x)$. To simplify, we consider the scalar electric field through the wave function $\psi(x)$ [16]. Thus, the wave equation for the electric field is similar to the

Schrödinger equation:

$$-\nabla^2\psi(x) - \delta\epsilon\frac{\omega^2}{c^2}\psi(x) = \bar{\epsilon}\frac{\omega^2}{c^2}\psi(x). \tag{2.25}$$

Comparing with equation 2.24, we observe that the term $\bar{\epsilon}\omega^2/c^2$ has the same functional form as the electron energy E, and $-\delta\epsilon\omega^2/c^2$ acts as a random potential, which causes the electromagnetic wave to scatter in the medium.

We note that $\epsilon(x)$ is positive; therefore, since $\bar{\epsilon}$ is an average, it will be positive in all cases. Consequently, $\bar{\epsilon}\omega^2/c^2$ is positive. When examining $\delta\epsilon\omega^2/c^2$, we observe its quadratic dependence on the frequency ω. Hence, by reducing the photon energy, namely its frequency ω, the disordered potential $-\delta\epsilon\omega^2/c^2$ decreases at the same rate. Unlike electron waves, in which localization is enhanced by decreasing the electron's energy, reducing the photon's energy leads to the complete disappearance of scattering, thus destroying the disorder. Because $\bar{\epsilon} + \delta\epsilon > 0$ must hold, light localizes within a specific frequency range, which differs from what occurs in electron localization [22].

As discussed in previous sections, coherent backscattering is a wave phenomenon and does not require a strongly disordered medium. Observing this phenomenon—where light diffusion is reduced due to interference—has stimulated an intensive search for Anderson localization of light. The first observations of coherent backscattering of light employed a rubidium atom gas (^{85}Rb). Further studies in cold atom gases showed that the Zeeman degeneracy of the atomic transition affects coherent transport, thereby reducing interference [23, 24, 25]. Moreover, unlike in the electron model, applying a magnetic field was found to restore the twofold increase in backscattering [26].

Currently, one of the advances in light localization research is the use of the Coupled Dipole Model (CDM), which has significantly deepened our understanding of the interactions between light and matter. This model addresses the light-mediated coupling between atoms arranged in a disordered manner and has enabled an accurate description of, for example, superradiance [27] and subradiance [28] in large atomic clouds. Although its equations are derived from quantum formalisms, in the linear optics regime (low pumping intensity), they take on a classical form, linking them to Maxwell's equations [12]. The CDM combines light interference with disordered atomic distributions, enabling detailed investigations of how Anderson localization occurs in photonic systems. This approach has led to significant progress in understanding 2D and 3D systems, as well as gaining deeper insight into polarization effects.

In the literature, there are measurements of light localization in 1D and 2D, a numerical example can be found in Appendix A. However, no measurements exist for light localization in 3D systems [11]. One of the experimental challenges involves clearly distinguishing localization from other effects, such as fluorescence and photon absorption. Moreover, a unique aspect of electromagnetic waves is their vector nature, which plays a crucial role in localization. In the work of S. E. Skipetrov and I. M. Sokolov [10],

the analysis of light localization in a 3D disordered medium was based on the scaling approach using the Thouless number g_{Th}. For the scalar model (which disregards near-field dipole-dipole interactions), there is a phase transition from extended to localized states. However, when considering the vector nature—i.e., the inclusion of near-field dipole-dipole interactions—no phase transition occurs. Thus, these configurations suggest that vector light Anderson localization cannot be achieved [10]. Similar results were also obtained in [29]. Hence, the vector characteristic inhibits Anderson localization of light in the case of resonant point scatterers, highlighting the importance of the electromagnetic wave's vector nature.

In this context, the work of C. E. Máximo and collaborators analyzed the Thouless number g_{Th}, borrowed from the electron model [12], applied it to a two-dimensional atomic cloud for both scalar and vectorial models. The choice to reduce dimensionality is justified because, under these conditions, there exist scattering channels with both a scalar and vectorial nature, and in addition, the computational power required to simulate this system is significantly lower. Thus, they concluded that for the scalar model, the conductance g_{Th} decays exponentially with increasing system size, as predicted by scaling theory. However, for the vectorial model, the conductance of the atomic cloud exhibits a slight decrease, remaining practically constant with increasing system size. This behavior contradicts scaling theory, which predicts that all 2D disordered scattering media should exhibit Anderson localization of light. It also shows that the effect of near-field terms makes this system delocalized.

In this dissertation, we will use the same 2D system in a disordered medium to study Anderson localization in the vectorial channel for a large number of particles. The motivation is to understand whether for low densities, when the contribution of near-field terms becomes negligible, localization can be restored. We will ensure that the cloud's radius is sufficiently large so that the near-field terms do not influence the system due to the large spacing. In this way, we will analyze how the conductance g_{Th} decays with increasing atomic cloud length.

In the next chapter, we begin by describing the model used by Maximo and presenting the approximations employed. This approach enables us to investigate the model under various regimes defined by atomic density and cloud length. Later in the chapter, we present the numerical methods and discuss each regime.

3 Model and numerical methods

As previously discussed, one way to quantify Anderson localization for light is by analyzing the dimensionless conductance when increasing the system size, based on scaling theory. A disordered medium can be modeled using an atomic cloud, described by the coupled-dipole model. A simplified description of the interaction between the radiation field and a two-level hydrogenic atom considers the wavelength λ of the radiation field to be much larger than the atomic de Broglie wavelength. Under this approximation, the atom plays the role of a point-like electric dipole.

Due to the vectorial nature of electromagnetic waves, angular momentum can be transferred to the atom. This effect becomes very influential in strongly disordered media, such as in Anderson Localization for light. Thus, the atoms have four allowed levels: a non-degenerate ground state $|g_j\rangle$ (angular momentum $\ell = 0$) and a triply degenerate excited state $|e_{j,m}\rangle$, where $m = 0, \pm 1$ indicate the possible projections of the angular momentum $\ell = 1$ along the quantization axis. An example can be visualized in Figure 4.

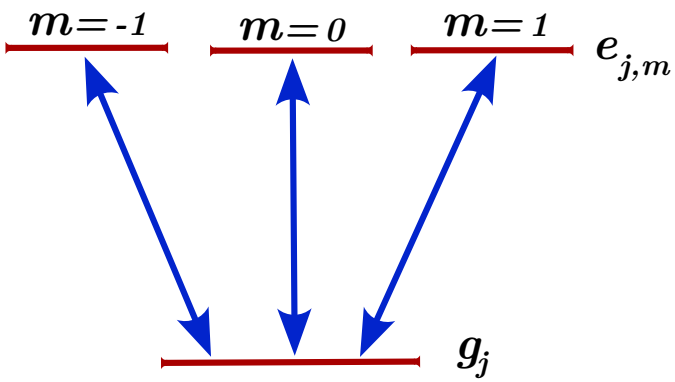

Figure 4 – Energy levels describing the scalar ($m = 0$) and vectorial ($m = \pm 1$) scattering channels of scattering. Three degenerate transitions are allowed.

Another approximation in the model is that, for low pumping intensity, the linear optics regime is implemented. That is, in this case, we are in the single-photon limit. Multi-excitations in the atomic system are neglected, and the total Hilbert space is restricted to the *single-excitation basis* $|g_1, \ldots, g_N\rangle, |e_{1,m}, g_2, \ldots, g_N\rangle, \ldots, |g_1, e_{2,m}, \ldots, g_N\rangle$. When considering all multiply-excited states the problem's complexity grows exponentially with system size. In the single-photon limit, the complexity grows linearly with system size.

Regarding the radiation field, Máximo's model assumes the propagation of free-space electromagnetic modes in a plane. Such a 2D geometrical constraint predicts a decoupling of the transition $m = 0$ from the others and generates two independent

propagation channels: one with polarization perpendicular to the plane of propagation (scalar) and another with polarization in that plane.

Rather than the typical application of a Zeeman magnetic field, such a dynamical decoupling arises from the 2D geometrical constraint imposed by the model. This situation can be generated by a cavity with very closely spaced mirrors.

Following the 2D model of propagation, we consider N atoms interacting with modes that propagate in the (x, y) plane (Fig. 5). The atoms are randomly distributed with an average homogeneous density $\rho = N/\pi R^2$.

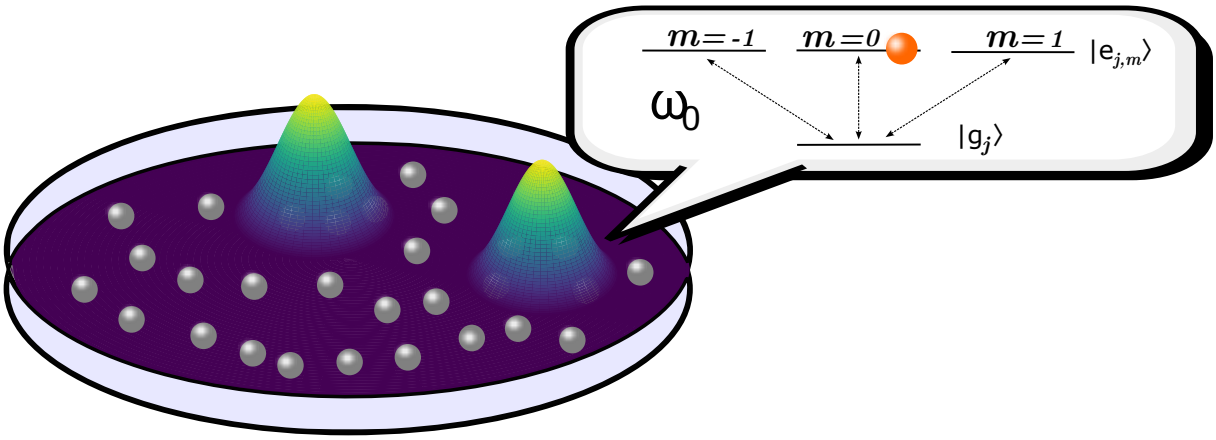

Figure 5 – Two-dimensional scattering scheme: the wave number k is confined in the plane (x,y).

In the scalar channel, the probability amplitude of a m=0 excited state is coupled only to the other m=0 states:

$$\frac{d\ \beta_j^{(0)}}{dt} = -\frac{\Gamma_0}{2}\ \beta_l^{(0)} - \frac{\Gamma_0}{2}\sum_{l=1}^{N} H_0(kr_{jl})\ \beta_l^{(0)}, \tag{3.1}$$

where H_n is the Hankel function of the first kind and order n. Here, $r_{jl} = \sqrt{x_{jl}^2 + y_{jl}^2}$ is the Euclidean distance between atom j and l. In the vector channel, as previously mentioned, the electric field of the light is in the plane of the atomic cloud, and the transitions m=+-1 evolve coupled through near-field terms:

$$\frac{d\ \beta_j^{(\pm1)}}{dt} = -\frac{\Gamma_1}{2}\ \beta_l^{(\pm1)} - \frac{\Gamma_1}{2}\sum_{l\neq j}\left[H_0(kr_{jl}) - e^{\mp 2i\varphi_{jl}} H_2(kr_{jl})\right]\ \beta_l^{(\pm1)}, \tag{3.2}$$

where $\tan\varphi_{jl} = (y_j - y_l)/(x_j - x_l)$ defines the angular coordinate for atom pair j and l. The decay rate for this channel is $\Gamma_1 = \Gamma_0/2$.

Interactions among dipoles in this atomic cloud produce collective scattering modes characterized by their decay rates, energies, and spatial extensions. Hereafter, we investigate the changes in these properties as the atomic density varies, as well as the scattering channel. We then verify these properties for different cloud configurations, considering both the scalar and vector channels.

3.1 Methods for the 2D Case

First, we discuss some spectral properties of our system, looking for a comparison between the scalar and vectorial cases. In the linear regime (that is, of a weak drive), the scattering properties of equations 3.1 and 3.2 can be encoded in the following matrix:

$$M^{2D}_{m,m'}(r_{jl}) = \delta_{m,m'}\left(\Gamma_0\delta_{m,0} + \Gamma_1\delta_{|m|,1}\right)\ H_0(kr_{jl}) + \Gamma_1\ \delta_{1,|m|}\ \delta_{m,-m'}\ e^{2im\varphi_{jl}}H_2(kr_{jl}), \quad (3.3)$$

where m, m' represent the states of the atoms in the atom pair j and l. When we choose the scalar channel, we set $m = m' = 0$. Consequently, the term $\delta_{1,|m|}$ equals zero, reducing the matrix to $M^{2D}_0(r_{jl}) = \Gamma_0\ H_0(kr_{jl})$.

Diagonalizing this matrix yields eigenvalues λ_n and eigenvectors ψ_n, where the decay rate $\gamma_n = \Re(\lambda_n)$ and energy $\omega_n = \Im(\lambda_n)$ are derived from the eigenvalues, according to $\lambda_n = \gamma_n + i\omega_n$. Hence, the family ω_n corresponds to the energy spectrum of the system. With the decay rate values γ_n we classify the modes into two groups. Subradiant modes ($\gamma_n < \Gamma_0$), which emit radiation slower than a single isolated atom, and superradiant modes ($\gamma_n > \Gamma_0$), with accelerated emissions.

Each eigenvector ψ_n is characterized by a probability density $|\psi^j_n|^2$, which corresponds to the probability of atom j being excited. A measure of the number of atoms contributing to the mode is given by the Inverse Participation Ratio (IPR), defined as:

$$\mathrm{IPR}_n = \frac{\sum_j |\psi^j_n|^4}{\left(\sum_j |\psi^j_n|^2\right)^2}. \quad (3.4)$$

The IPR quantifies the inverse of the number of atoms effectively involved in a mode. As the IPR value decreases, the number of atoms contributing to the mode increases. For example, an IPR value of 1/2 represents a mode where most of the weight comes from two atoms.

Furthermore, the eigenvectors ψ_n, have a center-of-mass position $\left(x^{\mathrm{CM}}_n, y^{\mathrm{CM}}_n\right)$, defined as:

$$x^{\mathrm{CM}}_n = \frac{\sum_j x_j|\psi^j_n|^2}{\sum_j |\psi^j_n|^2} \quad \text{and} \quad y^{\mathrm{CM}}_n = \frac{\sum_j y_j|\psi^j_n|^2}{\sum_j |\psi^j_n|^2}, \quad (3.5)$$

where x_j and y_j are the coordinates of atom j . The center of mass allows us to identify whether the mode belongs to the bulk or is close to the edge, and to determine the spatial decay from the center of mass. In particular, for Anderson-localized modes, the probability density is expected to decay as $|\psi^j_n|^2 \sim \exp\left(|r^{\mathrm{CM}}_n - r_j|/\xi\right)$, with ξ the localization length and $r^{\mathrm{CM}}_n = \sqrt{(y^{\mathrm{CM}}_n)^2 + (x^{\mathrm{CM}}_n)^2}$. We use a linear fit of the logarithm of $|\psi^j_n|^2$ to determine this quantity, which comes with a quality indicator of the fit, R^2. The quality factor R^2, which varies from 0 to 1, the closer to 1 the better the fit to the data.

Using the slope a obtained from this fit, we computed an auxiliary parameter α, given by $\alpha = -1/a$. This parameter represented the mode size and helped us determine whether we were within the limits discussed earlier regarding edge effects. We use α and R^2 to classify modes as localized. If and only if the auxiliary parameter is much smaller than the cloud radius ($\alpha \ll R$) and the quality indicator of the fit is greater than 0.5 ($R^2 < 0.5$). In this case, the auxiliary parameter is equal to the localization length ($\xi = \alpha$). However, if α is negative or greater than the cloud radius and the quality indicator of the fit is less than 0.5 ($R^2 > 0.5$), the mode is considered delocalized.

In the following sections, we discuss the properties introduced in this section, initially focusing on the interaction between atoms in the scalar case, as described in Equation 3.1. Subsequently, we analyze the interaction described by Eq. 3.2 , which accounts for the interaction to the vector case.

3.1.1 Scalar Case

We first consider Equation 3.1 to describe dipole interactions in the scalar case, looking for modes that exhibited Anderson localization.

By calculating the interactions within this atomic cloud and diagonalizing the matrix defined above Eq. 3.3 for the scalar channel, we obtained the system spectrum. This energy spectrum, represented in Figure 6, served as a mean to analyze the properties of each mode for this configuration of our system. The most subradiant modes ($\gamma_n < \Gamma_0$) exhibited IPR values greater than 1/10, although a continuous variation in values is observed. In other words, only a few atoms participated in these modes.

In contrast, the superradiant modes ($\gamma_n > \Gamma_0$) exhibited low IPR values, indicating that many atoms participate in these modes. Note that, we discarded modes with decay rates $\gamma_n < 10^{-14}$, which corresponds to the machine precision.

In Figure 7(a), we selected the most subradiant mode and represented its probability density. For this mode, the IPR is approximately 0.27, indicating that around 4 atoms effectively participate in this mode.

IPR values provided a first indication of whether modes is localized or not. Thus, in Figure 7(b), we show the probability $|\psi_n^j|^2$ as a function of the distance from the center of mass to atom j for the most subradiant mode. We observe an exponential decay of this probability. The linear fit yields $\alpha = 1.12$ with an R^2 greater than 0.5, indicating, by definition, a localized mode, since for this cloud $kR \approx 36$.

In Figure 7(c), in contrast to the previous case, we selected a superradiant mode and observed that the probability $|\psi_n^j|^2$ was spread throughout the cloud. Approximately 2130 atoms contributed to this mode, resulting in a low IPR value ($\approx 5.2\ 10^{-4}$). In Figure 7(d),

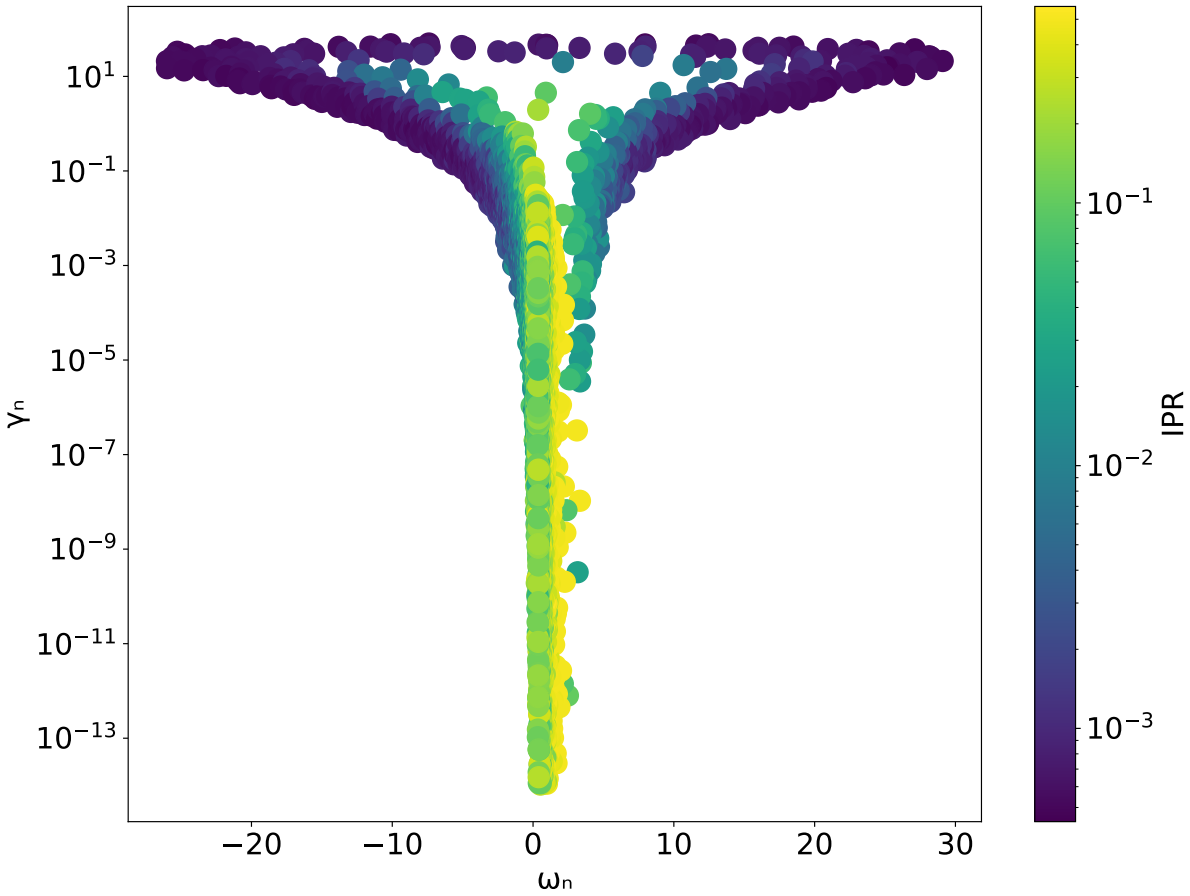

Figure 6 – (Color online) Inverse participation ratio of the scattering modes in the complex plane of the eigenvalues (γ_n, ω_n). Simulations were conducted for a homogeneous disk cloud of $N = 4000$ particles with a uniform density of $\rho/k^2 = 1$ for scalar light, therefore $kR \approx 36$.

the probability did not exhibit the exponential decay characteristic of Anderson localization and was approximately uniformly distributed across the cloud. The linear fit of these points yielded a negative auxiliary parameter and an R^2 value below 0.5.

In Figure 8(a), we show the linear fit of the logarithm of the probability for the most subradiant mode, with the points used for the fit in blue and the remaining points in black. To select the atoms contributing to the linear fit, we ordered the scatterers by increasing distance from the center of mass until the cumulative probability of these atoms exceeded 0.9999. Note that the eigenmodes are normalized, that is, $\sum |\psi_n^j|^2 = 1$. In Figure 8(b), we performed the same fit but included all atoms, the fit in (b) did not describe the exponential points well. Thus, we used the method from case (a) for all linear fits. The value of 0.9999 was chosen because it best fits the points with the largest weight, using the most subradiant mode to define the maximum probability sum.

We performed linear fits for all modes of our system and represented them in Figure 9(a) with the IPR. We observed that modes with lower auxiliary parameters α and $R^2 > 0.5$ are those with high IPR values. In Figure 9(b), we showed the decay rates, noting

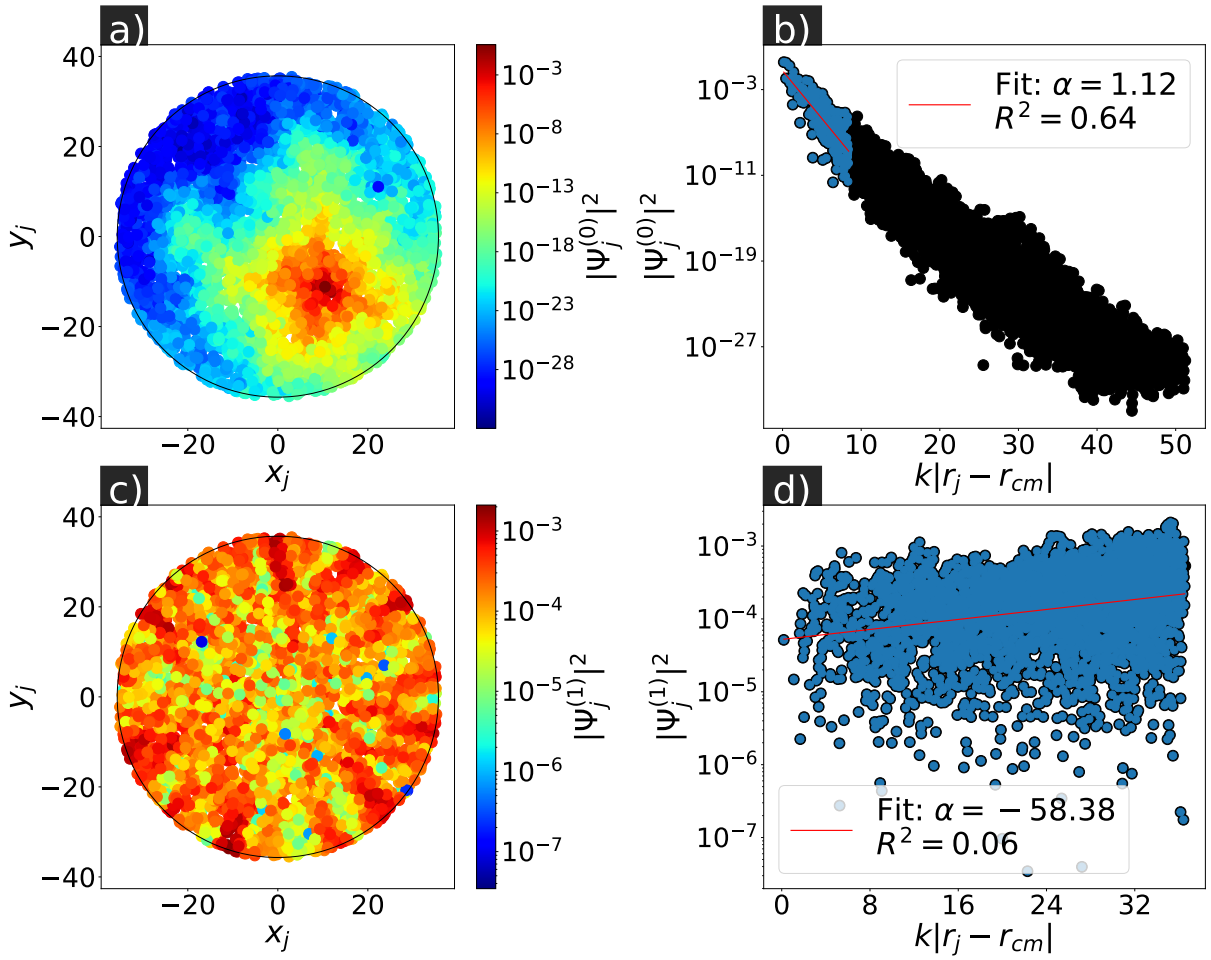

Figure 7 – (Color online) (a) The 2D profile and (b) the spatial profile as a function of the distance to the center of mass r_n^{CM} of the most subradiant mode (exponentially localized mode). (c) The 2D profile and (d) the spatial profile as a function of the distance to the center of mass r_n^{CM} of the superradiant mode (delocalized mode). Simulations were conducted for a homogeneous disk cloud of $N = 4000$ particles with a uniform density of $\rho/k^2 = 1$ for scalar light, therefore $kR \approx 36$.

that localized modes have $\gamma_n < 10^{-8}$. These figures highlighted the number of localized modes for the given system configuration.

Thus, we observed that in the scalar case, there are many modes which exhibit Anderson-like localization. We analyze properties such as the IPR, localization length ξ_n, decay rate γ_n, and the quality of the fit R^2. Localized modes exhibit high IPR values, small decay rates, and localization lengths much smaller than the cloud radius. Additionally, we identify superradiant modes, where the excitation probability is distributed throughout the entire atomic cloud.

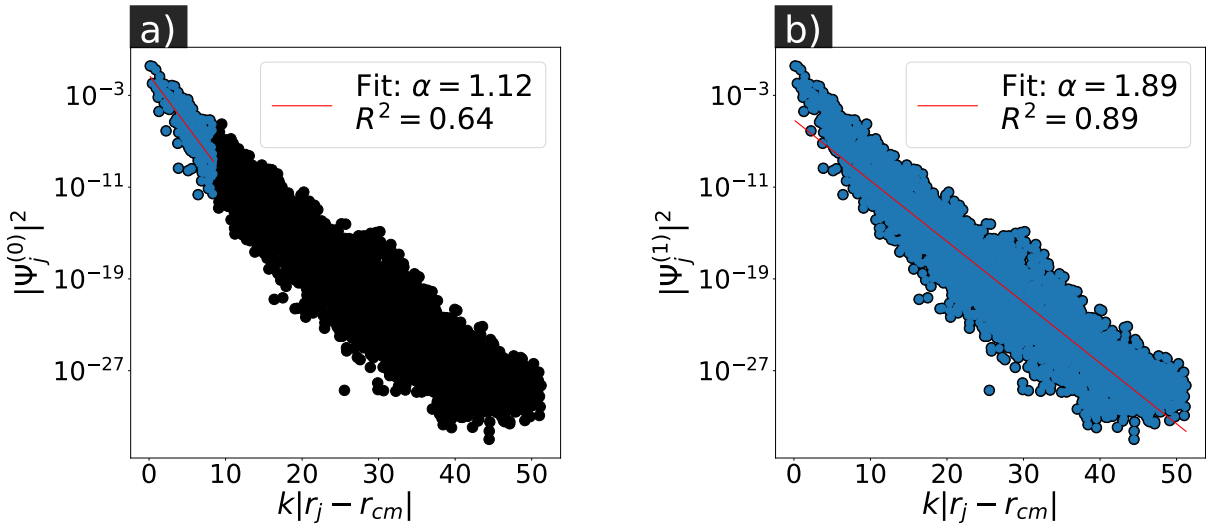

Figure 8 – (Color online) The atoms marked in blue represent the selected ones used to compute the fitting of the mode, the solid line. (a) The atoms selected add up to 99.99% of the total probability. (b) all atoms are selected. Simulations were conducted for a homogeneous disk cloud of $N = 4000$ particles with a uniform density of $\rho/k^2 = 1$ for scalar light, therefore $kR \approx 36$.

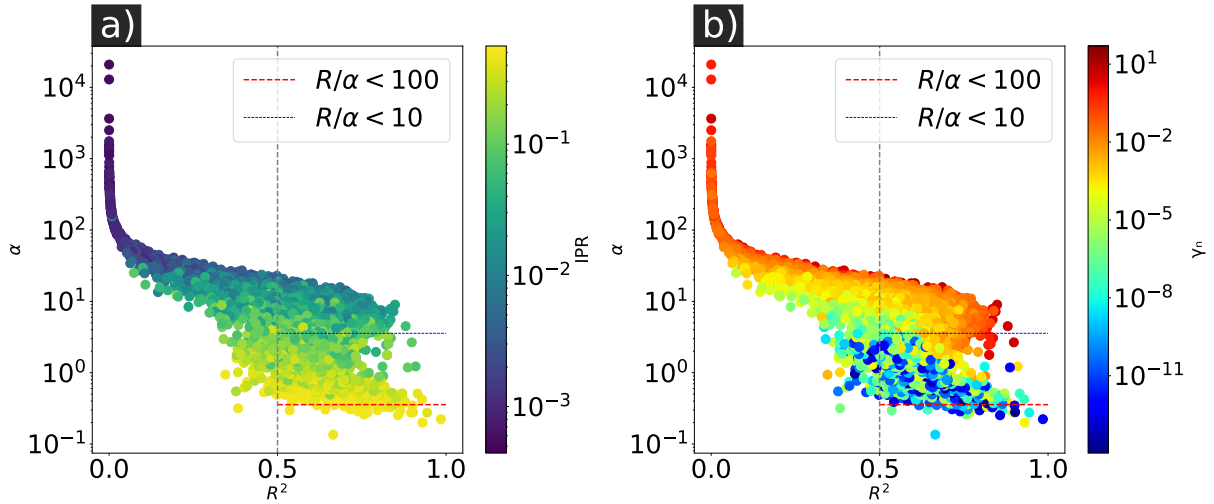

Figure 9 – (Color online) Values of auxiliary parameter (α_n), fitting coefficient (R^2), and (a) values of IPR and (b) decay rate (γ_n) for all modes. Simulations were conducted for a homogeneous disk cloud of $N = 4000$ particles with a uniform density of $\rho/k^2 = 1$ for scalar light, therefore $kR \approx 36$.

3.1.2 Vectorial Case

The 2D model enables the selective excitation of specific modes through the polarization of the incident electric field, thereby allowing control over the desired scattering behavior. This flexibility enables us to study the system under two different scenarios: a scalar model, where polarization effects are absent, and a vectorial model, where polarization plays an important role.

In this section, we calculate key properties of the system for the vectorial case. Specifically, we determine how polarization influences the localization length, decay rate, and the spatial profiles of the modes. By analyzing these properties, we aim to understand the distinct behaviors that arise due to the inclusion of polarization effects, providing a detailed comparison with the scalar case discussed previously.

For the vectorial case, we compute the interaction as described by equation 3.2. And diagonalizing the matrix defined above Eq. 3.3 for vectorial channel. To facilitate the comparison with the scalar case, we use the same atomic cloud configurations. As previously, the spontaneous emission rate of a single atom is set to $\Gamma_0 = 1$.

We repeat the process of calculating the eigenvalues and eigenvectors, incorporating near-field terms to better understand the influence of short-range interactions, and analyze the decay rate and energy of each mode, focusing on modes that fall above a specific threshold to ensure numerical stability. Specifically, we consider $\gamma_n > 10^{-14}$ to avoid issues related to machine precision.

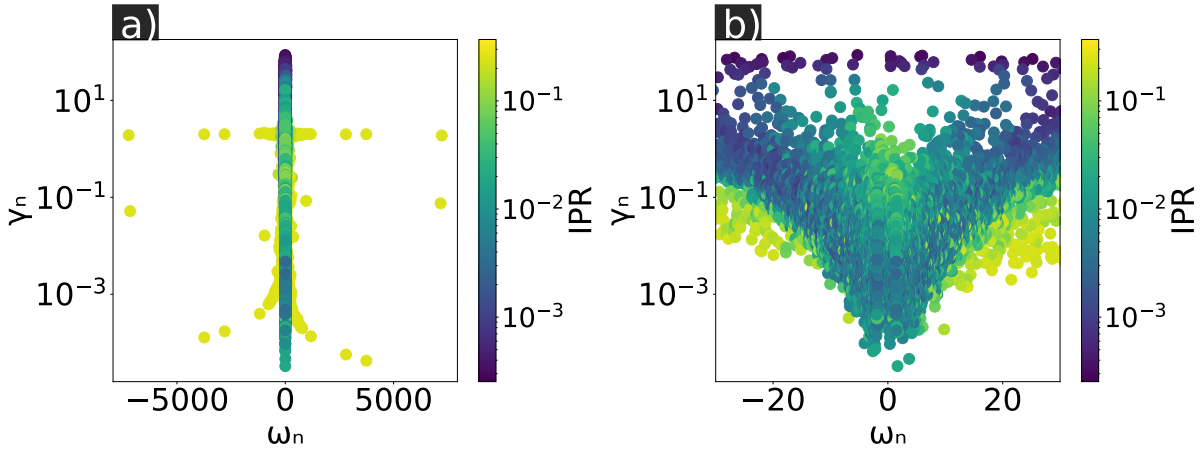

Figure 10 – (Color online) (a) Inverse participation ratio of the scattering modes in the complex plane of the eigenvalues (γ_n, ω_n) for vectorial light. (b) A zoomed-in view of (a). Simulations were conducted for a homogeneous disk cloud of $N = 4000$ particles with a uniform density $\rho/k^2 = 1$ for vectorial light, therefore $kR \approx 36$.

From the energy spectrum shown in Figure 10(a), we observed that, unlike the scalar case, there are modes with high energy ω_n and high IPR values. These modes are referred to as "pair modes"because the excitation probability is concentrated in a pair of atoms. We will discuss these pair modes in more detail in future sections; however, it is important to note that they are not exponentially localized.

To facilitate comparison with the scalar case presented earlier, Figure 10(b) provides a zoomed-in view. Since scalar case modes are mostly distributed near zero energy ($\omega_n \approx 0$), this zoom helps us visually compare the two cases.

Another difference in the spectrum of modes in the vector case is that the decay

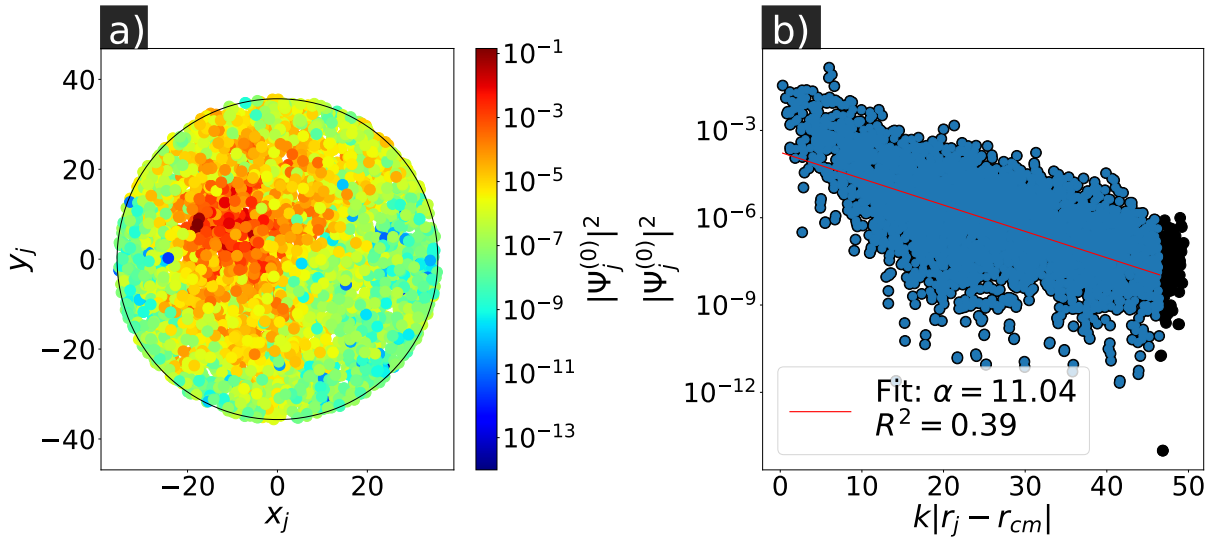

Figure 11 – (Color online) (a) Spatial profile as a function of the distance from the center of mass r_n^{CM} of the subradiant mode for vectorial light, and (b) the 2D profile of the same mode. Simulations were conducted for a homogeneous disk cloud of $N = 4000$ particles with a uniform density $\rho/k^2 = 1$, therefore $kR \approx 36$.

rates are about eight orders of magnitude higher than in the scalar case. In Figure 10(b),we also observe that most of these modes do not have high IPR values, indicating that, compared to the scalar case presented in the previous section, a larger number of atoms contribute to these modes.

To identify localized modes, as we did previously, we selected the most subradiant mode with energy close to zero. Figure 11(a) shows the effective contribution of each atom to this mode. We notice that more atoms participate in this mode than in the scalar case, resulting in a more distributed probability throughout the cloud. For this mode, the IPR is approximately 1.9 10^{-2}, suggesting that around 50 atoms effectively contribute. This number is about thirty times greater than in the scalar case but still lower than that of the superradiant mode in the scalar case.

Thus, observing only the IPR value is insufficient to determine whether a mode is localized, as discussed earlier. To verify this, we plot the probability as a function of the distance from the center of mass to atom j for this mode in Figure 11(b). The points exhibit an exponential decay. The linear fit gives $\alpha = 11.04$ and an R^2 value of 0.39, indicating that the mode is not localized, as the auxiliary parameter is only one-eighth of the cloud radius, and the quality indicator is less than 0.5. As discussed in the literature [12], Anderson localization is lost due to near-field effects present in the vector case interactions.

Similarly, we performed a linear fit for all modes in our system and represented the IPR values in Figure 12(a). We observed some modes with a quality factor close to 1, low auxiliary parameter values, and high IPRs; these are pair modes. Apart from these, we did not observe any modes with small auxiliary parameters α and $R^2 > 0.5$. Using

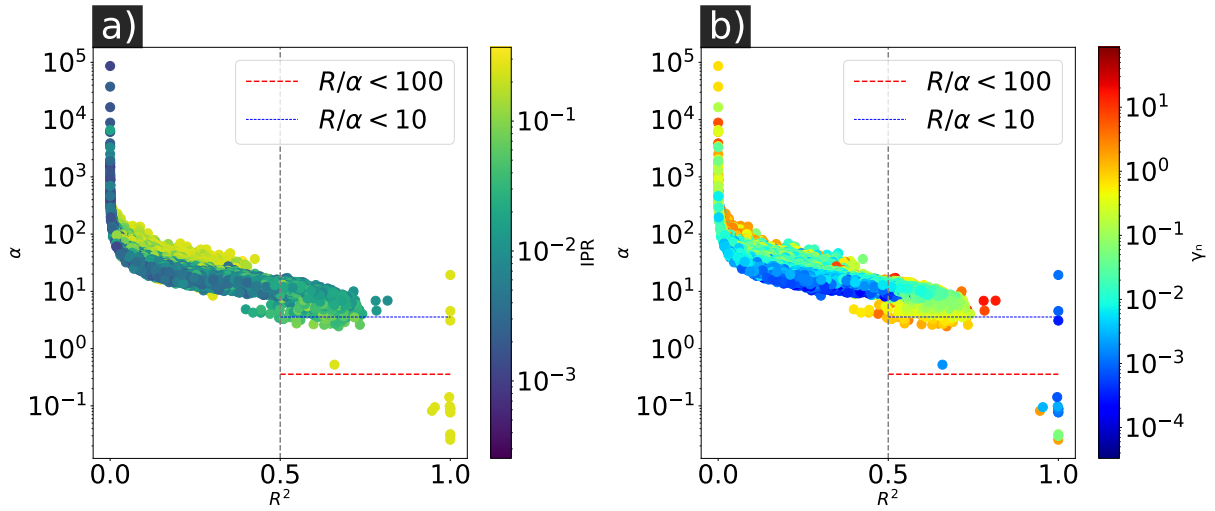

Figure 12 – (Color online) Values of the auxiliary parameter (α_n), fitting coefficient (R^2), and (a) values of IPR and (b) decay rate (γ_n) for all modes. Simulations were conducted for a homogeneous disk cloud of $N = 4000$ particles with a uniform density of $\rho/k^2 = 1$ for vectorial light, therefore $kR \approx 36$.

Figure 12(b) shows that, aside from the pair modes, the modes with the smallest auxiliary coefficients have decay rates close to 10^{-1}. Thus, we find no evidence of localized modes.

In this section, we calculated the main parameters needed to identify localized modes. These parameters include the IPR, the decay rates γ_n and energies ω_n and the probability of finding the excitation at each atom as a function of the distance from the center of mass.

Additionally, we analyzed how these parameters change between the scalar case, described by Equation 3.1, and the vector case, described by Equation 3.2. In the next section, we will study the decay rates and energies for atomic clouds at low densities, as well as the IPR and probability density.

3.2 System at Low Densities

In this section, we study the behavior of the variables analyzed earlier in the context of low densities. These variables include decay rates, energies of atomic clouds, the IPR, and probability density. This section focuses on highlighting the differences between high- and low-density cases. We first address the scalar case, followed by the vector case, maintaining the order of the previous sections.

3.2.1 Scalar Case

To obtain the eigenvalues and eigenvectors in the scalar case, we simulate a cloud with a density of $\rho/k^2 = 0.1$ and $N = 4000$, as in the previous chapters.

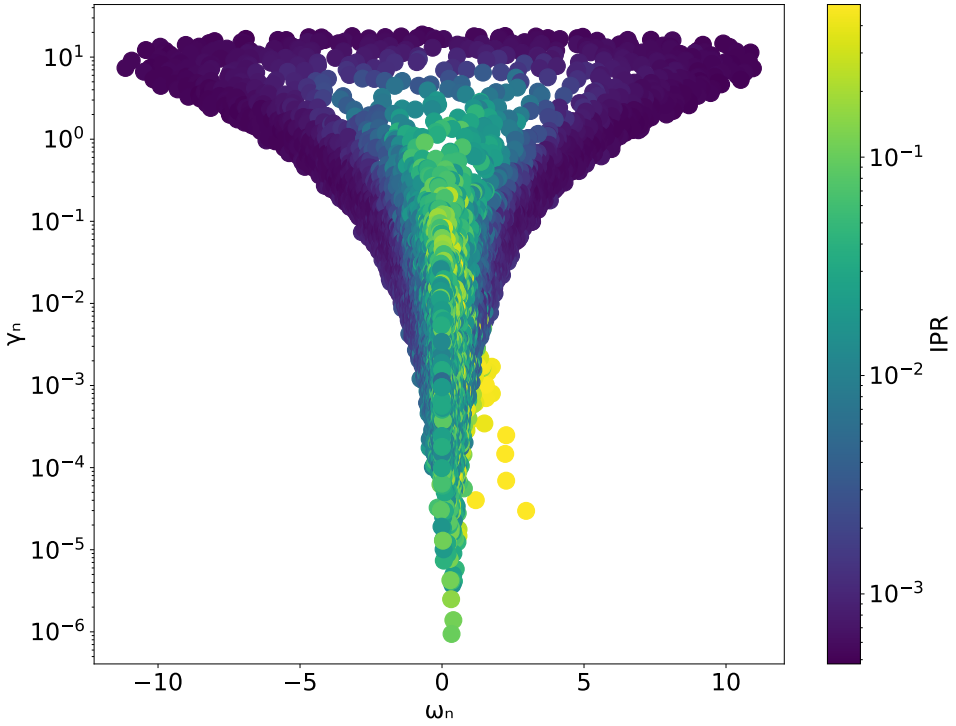

Figure 13 – (Color online) Inverse participation ratio of the scattering modes in the complex plane of the eigenvalues (γ_n, ω_n). Simulations were conducted for scalar light in a homogeneous disk cloud of $N = 4000$ particles with a uniform density of $\rho/k^2 = 0.1$, therefore $kR \approx 113$.

In Figure 13, we present the energy spectrum for the scalar case. Compared to the high-density system shown in Figure 6, the energy and decay rate intervals are much smaller, with decay rates spanning approximately eight orders of magnitude. Most modes exhibit low IPR values, indicating that they are likely delocalized.

To illustrate some of these modes, Figure 14(a) shows the spatial profile of the most subradiant mode. The probability density is concentrated in a specific region of the cloud. For this mode, the IPR is approximately 0.10, suggesting that around 10 atoms effectively contribute. Compared to the subradiant modes of the scalar case at a density of one, there is a slight increase in the number of scatterers, indicating that the probability density is more distributed in the dilute case.

In Figure 14(b), we also observe that the exponential decay is less pronounced than in the cases presented in the previous chapter. This is confirmed when we compare the values of the auxiliary parameter: $\alpha = 1.22$ for the dense case and $\alpha = 16.18$ for the dilute case. Additionally, in the low-density case, the quality factor of the fit is close to

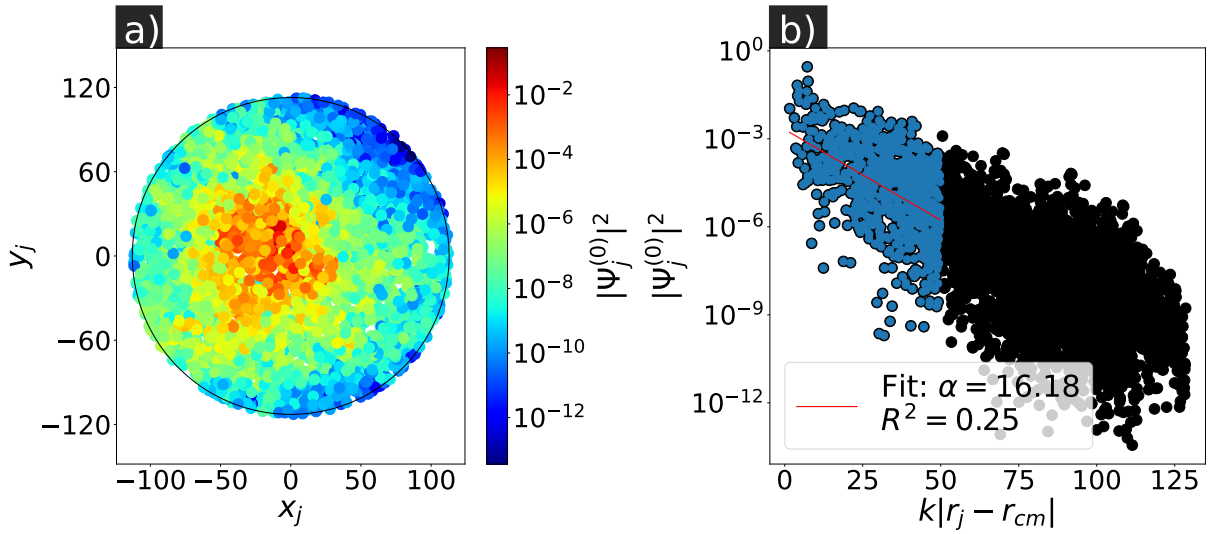

Figure 14 – (Color online) (a) Spatial profile and (b) 2D profile as a function of the distance from the center of mass r_n^{CM} of the subradiant mode for scalar light. (c) Spatial profile and (d) 2D profile characterized by large energy values ω_n. Simulations were conducted for a homogeneous disk cloud of $N = 4000$ particles with a uniform density of $\rho/k^2 = 0.1$, therefore $kR \approx 113$.

zero. Comparing the auxiliary parameter with the cloud radius, we find that the auxiliary parameter is about five times smaller.

We conclude that since the auxiliary parameter is of the same order of magnitude as the atomic radius, and the value of R2 is less than 0.5. Therefore the subradiant mode does not exhibit localization.

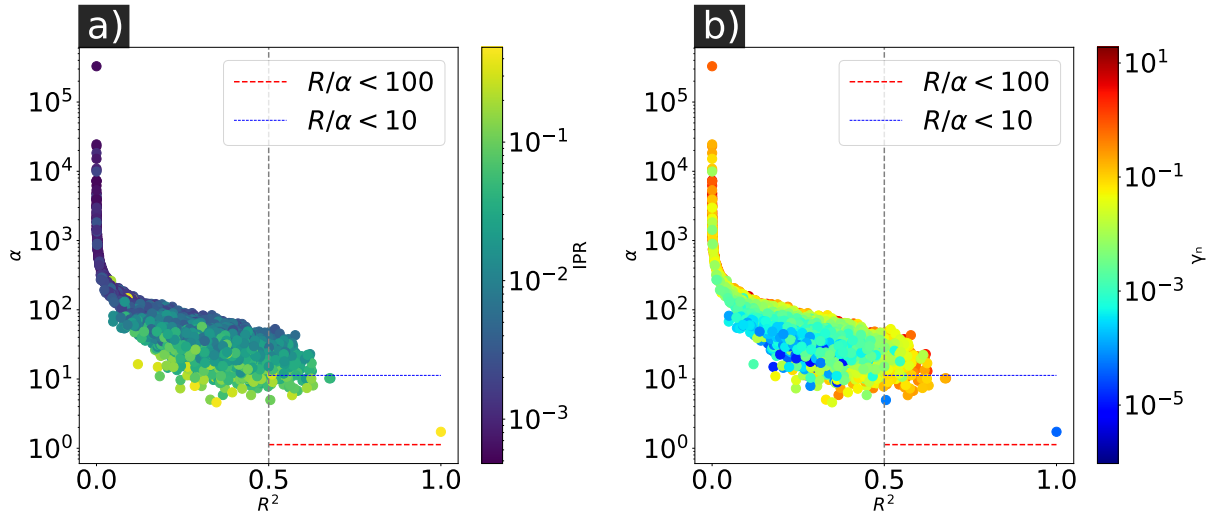

Figure 15 – (Color online) For all modes, the values of the auxiliary parameter (α_n), fitting coefficient (R^2), (a) IPR values, and (b) decay rates (γ_n) are presented. Simulations were conducted for scalar light in a homogeneous disk cloud of $N = 4000$ particles with a uniform density of $\rho/k^2 = 0.1$, therefore $kR \approx 113$.

Similarly, we performed a linear fit for the most subradiant mode. In Figure 15(a), we plot, for all modes, the IPR values, the auxiliary parameter, and the quality factor of

the fit. We observe a few modes with $R^2 > 0.5$, but their auxiliary parameter values are not significantly smaller than the cloud radius. Figure 15(b) shows that these modes with higher quality factors do not necessarily have the lowest decay rates.

In this case, localized modes were predicted; however, no localized modes were observed. This can be explained by the fact that the localization length for this density exceeds the radius of the cloud. In the next section, we study the behavior of the system in low-density conditions with vector light, focusing on the auxiliary parameter for different modes.

3.2.2 Vector Case

For the calculations in the vector case, we used the cloud configuration from the previous case. As before, we obtain the spectrum for this specific case, shown in Figure 16.

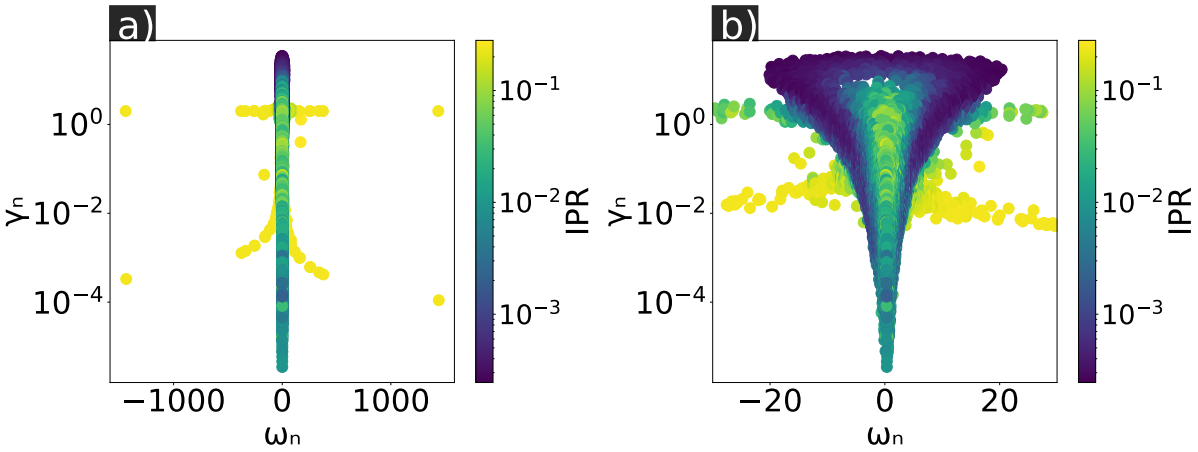

Figure 16 – (Color online) Inverse participation ratio of the scattering modes plotted in the complex plane of the eigenvalues (γ_n, ω_n). Simulations were conducted for vector light in a homogeneous disk cloud of $N = 4000$ particles with a uniform density of $\rho/k^2 = 0.1$, therefore $kR \approx 113$.

Following the procedure from previous chapters, we select the most subradiant mode from the spectrum in Figure 16(a). Compared to the high-density vector case, the decay rates are two orders of magnitude lower. However, these decay rates are still about eight orders of magnitude higher than those in the dense scalar case.

Regarding the IPR values, we observed that the highest IPR values still correspond to the pair modes, unlike in previous cases. This can be verified in Figure 17(a), where the probability of this mode is spread throughout the cloud.

In Figure 17(b), we present the spatial profile of this subradiant mode. The auxiliary parameter is approximately one-fifth of the cloud radius, and the quality factor of the fit is greater than 0.5, although the decay does not clearly follow an exponential trend.

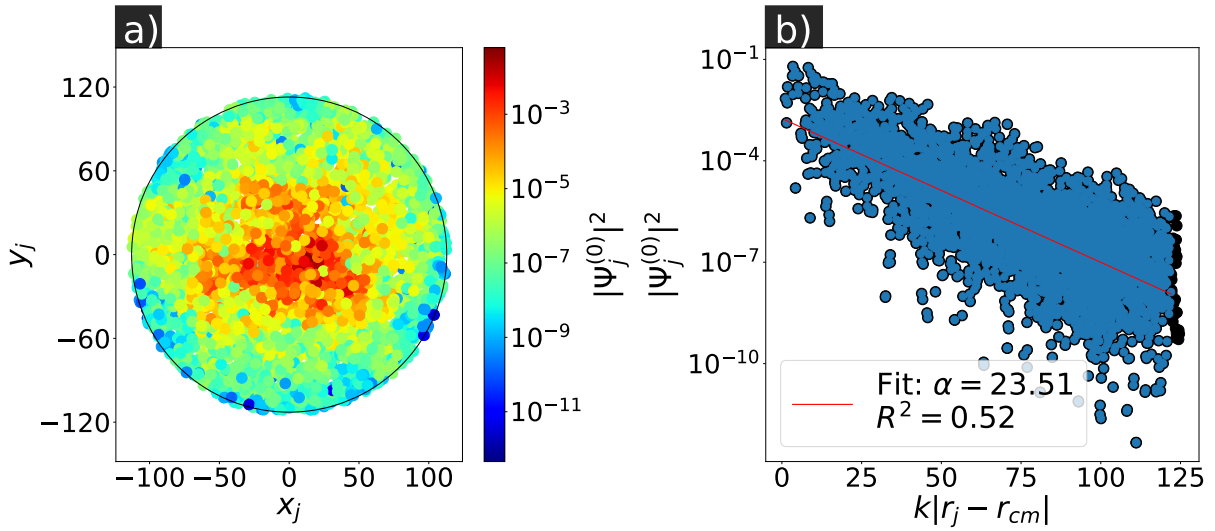

Figure 17 – (Color online) (a) Spatial profile and (b) 2D profile as a function of the distance from the center of mass r_n^{CM} of the subradiant mode for vector light. (c) Spatial profile and (d) 2D profile characterized by large energy values ω_n. Simulations were conducted for vector light in a homogeneous disk cloud of $N = 4000$ particles with a uniform density of $\rho/k^2 = 0.1$, therefore $kR \approx 113$.

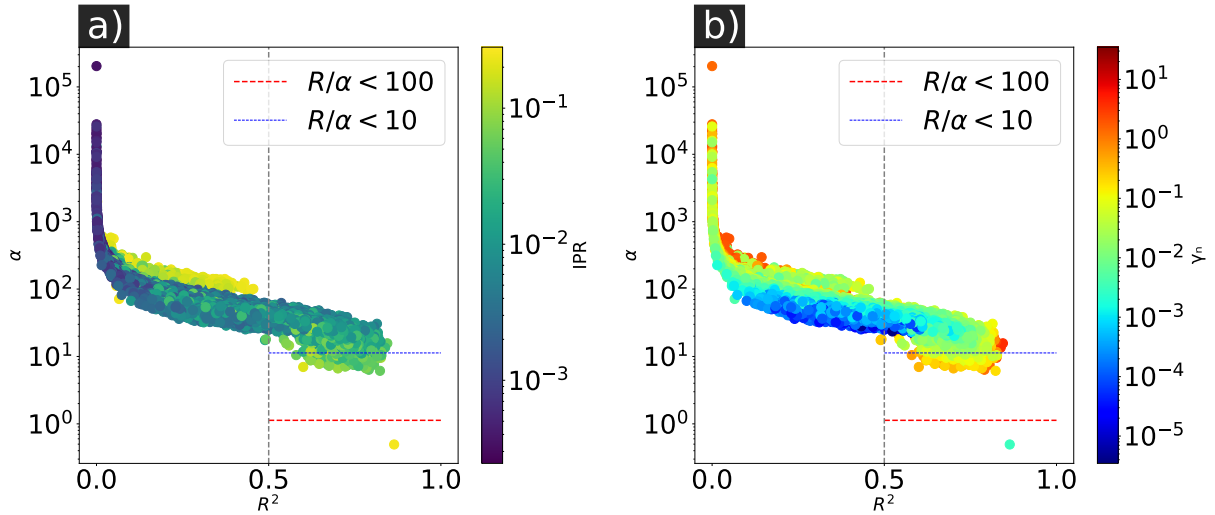

Figure 18 – (Color online) Values of the auxiliary parameter (α_n), fitting coefficient (R^2), (a) IPR values, and (b) decay rates (γ_n) for all modes. Simulations were conducted for vector light in a homogeneous disk cloud of $N = 4000$ particles with a uniform density of $\rho/k^2 = 0.1$, therefore $kR \approx 113$.

In Figure 18(a), we perform a linear fit for all modes and plot the IPR values, auxiliary parameters, and quality factors. We observed that modes with $R^2 > 0.5$ do not have auxiliary parameters significantly smaller than the cloud radius. Using Figure 18(b), we see that these modes with higher quality factors do not necessarily have the smallest decay rates, similar to what we observed in the previous case. Thus, we do not observe any localized modes.

When we compare this figure with the dense case in the vector model, we see

fewer pair modes.This is likely because the atoms are more widely spaced at lower density, preventing the formation of many pair modes.

In conclusion, at low densities, we do not observe localized modes in either the scalar or vector cases. The main reason for not observing localization in the scalar case at this low-density regime is that the auxiliary parameter is of the same order of magnitude as the system's radius. A possible solution would be to increase the system's radius, thereby increasing the number of scatterers. However, due to computational limitations such as memory and simulation time, we opted to vary the density while keeping the maximum number of atoms constant.

The density of the cloud plays a crucial role, especially when analyzing the conductance of the system. In the following sections, we calculate this property, starting by examining how conductance changes with different cloud radii. We then analyze how this property varies across different density ranges, with a particular focus on the low-density limit.

3.3 Conductance

In previous chapters, we introduced the property of conductance, also referred to as the Thouless number. In this section, we will initially calculate it for the systems presented in the earlier sections. Subsequently, we will analyze how the conductance is influenced by an increase in radius while maintaining constant densities. Finally, we will discuss how conductance varies across different density ranges.

The conductance is associated with the average decay rates and the energy differences between modes. It is defined as:

$$g = \left\langle \frac{1}{\gamma_n} \right\rangle^{-1} / \langle \omega_n - \omega_{n-1} \rangle \ ,$$

where γ_n is the decay rate, ω_n represents the energy for mode n, and ω_{n-1} denotes the energy of the mode preceding mode n,where the denominator corresponds to the average of the energies differences in ascending order.

Initially, we selected atomic clouds with a calculated density of $\rho/k^2 = 1$ and $N = 4000$, corresponding to a radius of $kR \approx 35$. For the scalar case (see Fig.6), the average conductance is $g \approx 10^{-11}$. In contrast, for the vector case (see Fig. 10), the conductance is $g \approx 10^{-2}$. When comparing conductance values across different cases, the lowest conductance is observed in the scalar case with a density of $1/k^2$, which is the largest value of density simulated. This finding suggests that, under these configurations, the cloud is less conductive compared to other cases. This behavior can be attributed to the presence of numerous localized states in this configuration, which confine the excitation within

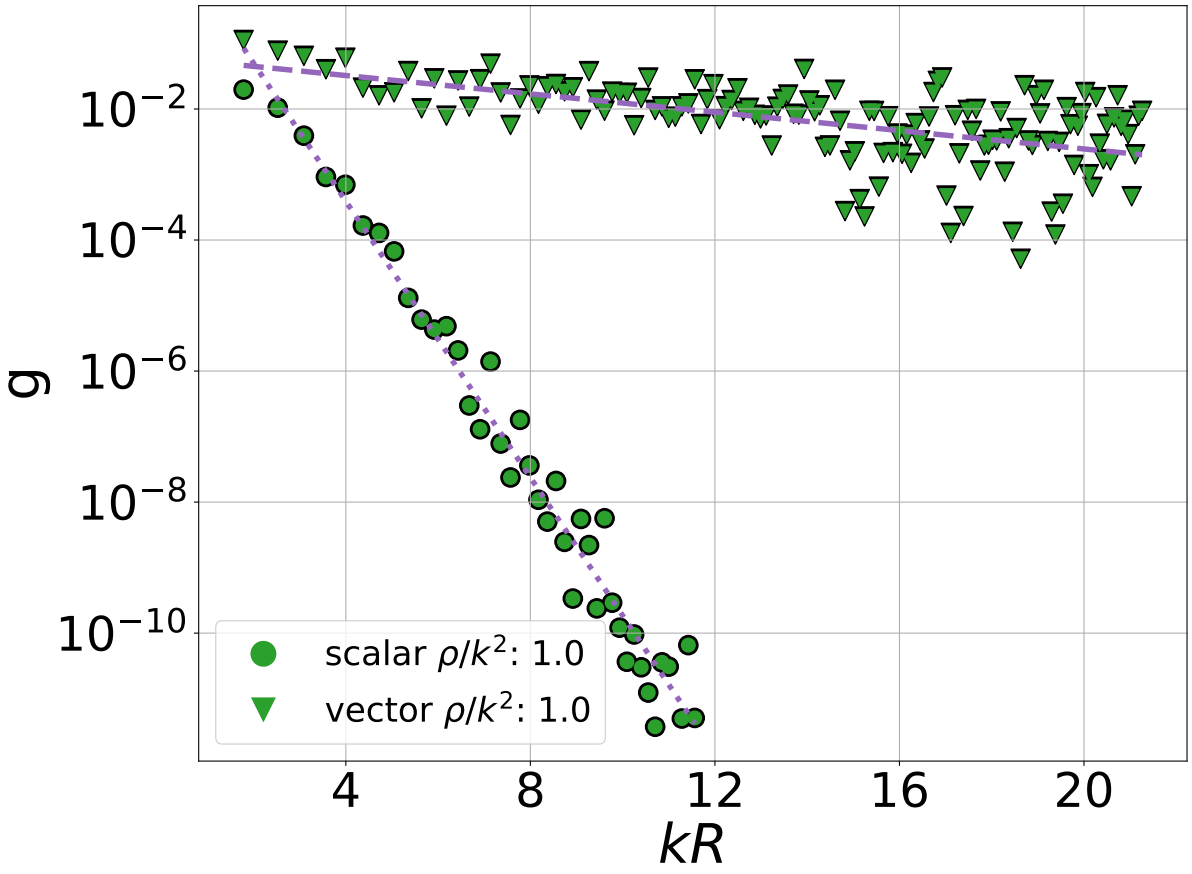

Figure 19 – Conductance for atomic clouds with a density $\rho/k^2 = 1$ (green) for the vector channel (triangles) and the scalar channel (circles). The number of atoms ranges from 20 atoms to 910 atoms, and the number of realizations from 10 to 1.

the cloud. In the vectorial case, the conductance is significantly higher, indicating that the excitation traverses the cloud without being trapped. The difference in conductance between the scalar and vector cases is approximately nine orders of magnitude.

This also happens when we calculate the average conductance for different values of cloud radius, as shown in Figure 19. We note that in the dense regime ($\rho/k^2 = 1$), for the scalar case represented by circles, the conductance decreases exponentially with increasing radius. For example, at $kR \approx 10$, the conductance is $g \approx 10^{-10}$. In the vector case, represented by triangles, the conductance slightly decreases with increasing cloud radius, in agreement with the literature [12]. The microscopic explanation is that the absence of localized allows transport through the cloud. Therefore, the conductance of the scalar channel shows a sharper decline compared to the vector channel as we increase the cloud radius. For the dilute cases, where the cloud has a density $\rho/k^2 = 0.1$ and $N = 4000$, corresponding to a radius of $kR \approx 113$, the average conductance for the scalar case is $g \approx 10^{-2}$.

For the vector case, the conductance is $g \approx 10^{-3}$. The difference between the two

regimes of density decreases to about one order of magnitude. In this scenario, unlike the previous cases, the conductance in the vector channel is lower than in the scalar channel, indicating a lower probability of transport within the vectorial channel.

To investigate Anderson localization in the vector channel, the study focuses on low-density regimes and large atomic cloud radii, as fewer atoms are required to achieve larger radii at lower densities. In the subsequent section, conductance is calculated as a function of cloud radius for two density values, providing insights into its behavior in low-density regimes.

3.4 Conductance at Different Densities

In this section, we calculate the conductance as a function of the cloud radius for different density values. Figure 20 illustrates the conductance g for two distinct density regimes. The first regime is a denser case ($\rho/k^2 = 0.3$), represented in blue, while the second is the dilute case ($\rho/k^2 = 0.1$), represented in red. Additionally, the vector and scalar channels are indicated by triangles and circles, respectively. In the dense case within the scalar channel, we observe that conductance decreases exponentially with increasing radius. As discussed previously, this behavior indicates a significant number of localized modes, resulting in conductance values approaching $g \approx 10^{-10}$ for $kR = 50$. In the dense case for the vector channel, we observe a slight decrease in conductance g compared to the scalar model. The difference in conductance between the two channels is approximately eight orders of magnitude for $kR \approx 50$.

Regarding the conductance for the dilute atomic cloud ($\rho/k^2 = 0.1$), represented in red, the scalar case exhibits a slight decrease, differing from the dense case. For an atomic cloud radius of $kR \approx 50$, the conductance is approximately 10^{-1}. When examining the vector channel, we find conductance values lower than those in the scalar case. For $kR \approx 75$, for example, the conductance is approximately 10^{-2}. Therefore, in addition to the magnitude of the difference between the conductances of the scalar and vector channels being smaller, the vector channel conductance remains lower than that of the scalar channel, unlike what was observed in the dense case. This can be explained by the fact that in the vector channel, the system is not in the localized regime due to the near-field terms, as already explained in the literature [10, 12]. Consequently, light has more channels to propagate.

Based on the scaling theory discussed in previous chapters, which predicts that every two-dimensional disordered system will enter a localized regime for sufficiently large systems and any degree of disorder, we infer that if the cloud radius is sufficiently dilute, since the near-field terms do not influence the system, one may reach a localized regime in

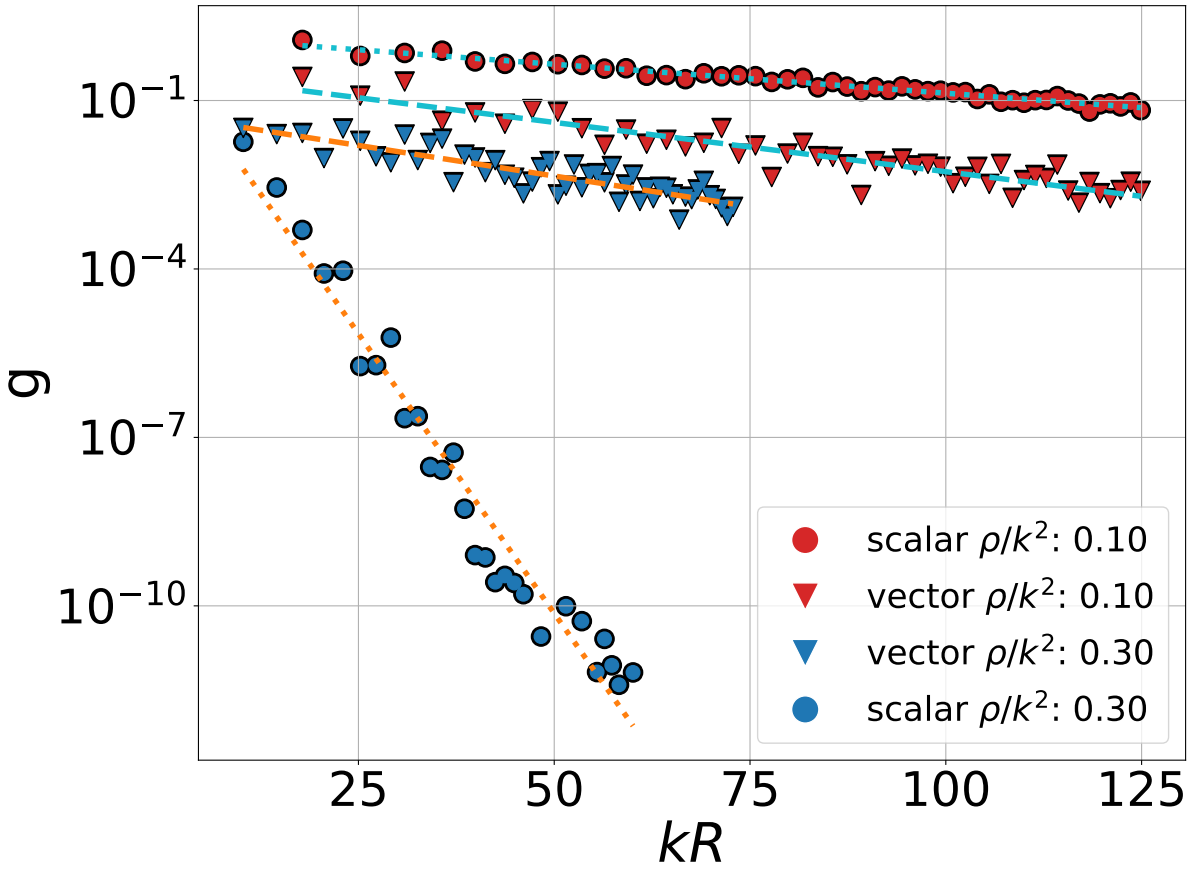

Figure 20 – Conductance for atomic clouds with a density of $\rho/k^2 = 0.1$ (red) and $\rho/k^2 = 0.3$ (blue) for vector channels (triangles) and scalar channels (circles). The number of atoms ranges from 20 to 910, and the number of realizations ranges from 5 to 1.

the vector channel. To determine the density at which the conductance g of the vector channel becomes small (i.e., where the system enters the localized regime), we use the linear fits shown in Figure 20. By extending these curves up to $kR = 1000$, we obtain Figure 21. In this figure, the conductance for the dense case in the vector channel (blue triangles) approaches 10^{-10} at $kR \approx 400$. Meanwhile, for the dilute case in the vector channel (red triangles), it approaches 10^{-10} at $kR \approx 500$. Although the dense case ($\rho = 0.3$) in the vector channel has a smaller radius value than the dilute case ($\rho/k^2 = 0.1$), we must consider the number of scattering particles required to achieve such a cloud size, recalling that $N = \pi\,(kR^2)\,\rho$. For the dense case vector channel to reach $kR = 400$, more than $1.5\ 10^5$ particles are required. Meanwhile, for the dilute vector channel, approximately $7.8\ 10^4$ particles are sufficient to reach $kR \approx 400$. The time required to diagonalize this matrix is proportional to the matrix size cubed. In Appendix 1, we present a table detailing the simulation time for different matrix sizes, programming languages, and computers.

The matrix size depends on the channel being analyzed for conductance. In scalar channels, the matrix size is $N \times N$. However, for the vector channel, the matrix size is $2N \times 2N$. Indeed, a challenge faced is RAM memory, which limits the system size that can

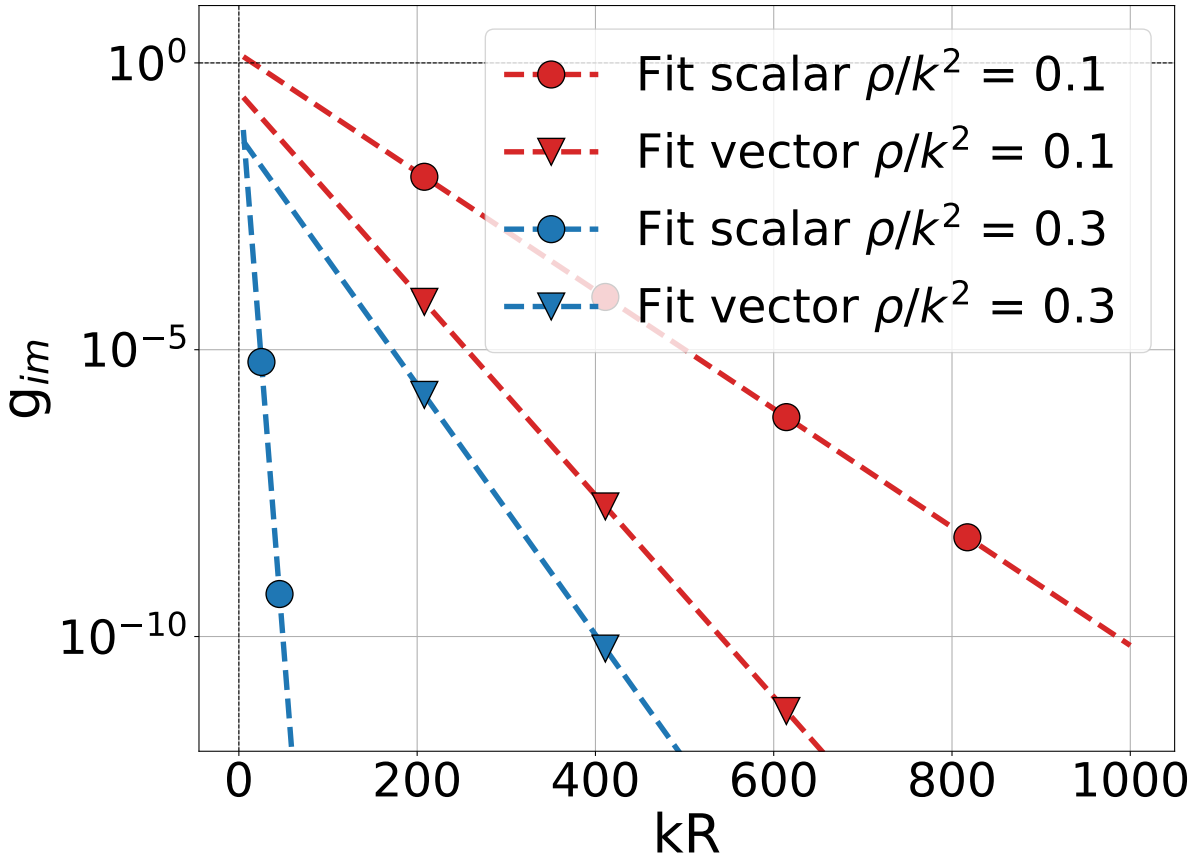

Figure 21 – Using the parameters obtained from the linear fit in Figure 20, we predict the conductance for clouds with kR up to 1000. The prediction for the dense cloud ($\rho/k^2 = 0.3$) is shown in blue, and the prediction for the dilute cloud ($\rho/k^2 = 0.1$) is shown in red. The scalar channel is represented by circles, while the vector channel is represented by triangles for both density regimes.

be simulated. To address this issue, we utilized the computing cluster at UFSCar. Although the matrix diagonalization rate in the cluster is lower than that of newer computers, the cluster offers a large memory capacity. This abundance of memory distributed over several nodes enables the simultaneous diagonalization of multiple matrices and, thus, statistics over many realizations. The maximum limit achieved to compute a conductance realization in the vector channel was with 3.5 10^4 particles ($kR \approx 300$). The time required to perform this calculation exceeded 46 hours. Based on the data presented in Appendix B, we estimate that the diagonalization of a matrix corresponding to 7.8 10^4 particles in the vector channel would take approximately 26 days to complete. At the peak of this simulation, the memory utilized would exceed 900 GB. This calculation is not impossible but is computationally expensive. Finally, all the images and calculations presented were computed using Python and an example code can be found in Appendix C.

4 Conclusion

In this work, we conducted a search for localized modes in the context of Anderson localization for light, considering the vector versus scalar channels in two-dimensional systems. Initially, we reviewed the existing literature, addressing the phenomenon of coherent backscattering, which occurs when a wave is scattered in weakly disordered media. This effect is crucial to corroborate Anderson localization since it arises due to the wave-like nature of the system. Anderson localization was originally formulated to explain the metal-insulator transition in materials. However, it has been observed that Anderson localization occurs for all types of waves scattered in strongly disordered media. Additionally, localized modes are those that exhibit an exponential decay up to a certain length, known as the localization length. Furthermore, based on concepts in condensed matter physics, it is possible to measure the location using the dimensionless conductivity g. This quantity strongly depends on the size and dimensionality of the studied sample. Using the dimensionless conductance g, we observed that this parameter also controls the behavior of the system, thus leading to the development of the scaling theory. Subsequently, we studied some concepts underlying Anderson localization for light. Light possesses unique properties when compared to the "quantum wave"(electrons). The polarization of light causes near-field terms to inhibit Anderson localization. For this reason, there is no conclusive evidence of this phenomenon in disordered 3D systems. In 1D and 2D systems, according to the scaling theory, Anderson localization is expected to always occur. Nonetheless, studies have shown that when considering light polarization in disordered two-dimensional systems, near-field terms also inhibit localization. Thus, we sought a regime where near-field terms do not affect Anderson localization, that is, the dilute regime of two-dimensional systems.

Additionally, we studied some parameters that can indicate Anderson localization, such as the decay rate and the Inverse Participation Ratio. We examined how these parameters change for different density regimes and for the two different channels. Using these parameters, we can classify when a mode is localized, as its wavefunction should exhibit exponential decay. Furthermore, when observing the parameters mentioned above, we noted that localized modes exhibit a high spontaneous decay rate, and few atoms participate in these modes, unlike extended modes.Another parameter of great importance in our study was the dimensionless conductance. It is predicted that when localized modes are present, conductance should decrease with the increasing size of the system. For dense systems, we observed that in the scalar channel, localized modes dominate for small atomic cloud lengths, leading to conductance approaching zero (insulator). In the vectorial channel, however, conductance remains nearly constant. Nevertheless, in larger atomic clouds, a

slight decrease in conductance is observed. This slight reduction in the vectorial channel conductance motivated us to study the effects of large atomic clouds on conductivity, aiming to find localized modes for a 2D system in the vectorial channel.

Thus, we performed computational calculations for dilute systems to achieve the largest possible atomic cloud radius. The results showed that, in the dilute regime, conductance in the vectorial channel is lower than in the scalar channel; this behavior is not observed in the dense regime. Based on these results, we extrapolated the atomic cloud radius at which exponentially localized modes may exist in the vectorial channel. However, achieving this cloud size requires simulations involving tens of thousands of atoms, which imply long execution times and high computational memory costs. For future projects, optimizing memory usage by eliminating unnecessary variables may reduce memory demands, although this might increase simulation time. Another optimization possibility involves exploring high-performance programming languages. In our study, several languages were evaluated, and Python emerged as the most efficient; thus, it was chosen. Another potential development involves performing matrix diagonalization using graphics processing units (GPUs), which are already employed for this type of computation.

References

1 ANDERSON, P. W. Absence of diffusion in certain random lattices. *Physical review*, APS, v. 109, n. 5, p. 1492, 1958.

2 MÜLLER, C. A.; DELANDE, D. Disorder and interference: localization phenomena. *arXiv preprint arXiv:1005.0915*, 2010.

3 ABRAHAMS, E. pw anderson, dc licciardello and tv ramakrishnan. *Phys. Rev. Lett*, v. 42, p. 673, 1979.

4 THOULESS, D. Localization distance and mean free path in one-dimensional disordered systems. *Journal of Physics C: Solid State Physics*, IOP Publishing, v. 6, n. 3, p. L49, 1973.

5 ABOU-CHACRA, R.; THOULESS, D.; ANDERSON, P. A selfconsistent theory of localization. *Journal of Physics C: Solid State Physics*, IOP Publishing, v. 6, n. 10, p. 1734, 1973.

6 KRAMER, B.; BERGMANN, G.; BRUYNSERAEDE, Y. *Localization, Interaction, and Transport Phenomena: Proceedings of the International Conference, August 23–28, 1984 Braunschweig, Fed. Rep. of Germany*. [S.l.]: Springer Science & Business Media, 2012. v. 61.

7 STÖRZER, M. et al. Observation of the critical regime near anderson localization of light. *Physical review letters*, APS, v. 96, n. 6, p. 063904, 2006.

8 WIERSMA, D. S. et al. Localization of light in a disordered medium. *Nature*, Nature Publishing Group UK London, v. 390, n. 6661, p. 671–673, 1997.

9 GJONBALAJ, N. O.; OSTERMANN, S.; YELIN, S. F. Modifying cooperative decay via disorder in atom arrays. *Physical Review A*, APS, v. 109, n. 1, p. 013720, 2024.

10 SKIPETROV, S. E.; SOKOLOV, I. M. Absence of anderson localization of light in a random ensemble of point scatterers. *Physical review letters*, APS, v. 112, n. 2, p. 023905, 2014.

11 SKIPETROV, S. E.; PAGE, J. H. Red light for anderson localization. *New Journal of Physics*, IOP Publishing, v. 18, n. 2, p. 021001, 2016.

12 MÁXIMO, C. E. et al. Spatial and temporal localization of light in two dimensions. *Physical Review A*, APS, v. 92, n. 6, p. 062702, 2015.

13 CHABANOV, A.; STOYTCHEV, M.; GENACK, A. Statistical signatures of photon localization. *Nature*, Nature Publishing Group UK London, v. 404, n. 6780, p. 850–853, 2000.

14 FAYARD, N. et al. Many-body localization in waveguide quantum electrodynamics. *Physical Review Research*, APS, v. 3, n. 3, p. 033233, 2021.

15 PING, S. Mesoscopic phenomena. *Introduction to Wave Scattering, Localization and Mesoscopic Phenomena*, Springer, p. 297–322, 2006.

16 CIPRIS, A. *Long-lived collective modes of light in cold atoms: experimental and numerical studies on subradiance and Anderson localization*. Tese (Doutorado) — Université Côte d'Azur, 2022.

17 AEGERTER, C. M.; MARET, G. Coherent backscattering and anderson localization of light. *Progress in Optics*, Elsevier, v. 52, p. 1–62, 2009.

18 LAGENDIJK, A.; TIGGELEN, B. v.; WIERSMA, D. S. Fifty years of anderson localization. *Physics today*, AIP Publishing, v. 62, n. 8, p. 24–29, 2009.

19 BRANDES, T.; KETTEMANN, S. *Anderson localization and its ramifications: Disorder, phase coherence, and electron correlations*. [S.l.]: Springer Science & Business Media, 2003. v. 630.

20 WEGNER, F. J. Electrons in disordered systems. scaling near the mobility edge. *Zeitschrift für Physik B Condensed Matter*, Springer, v. 25, n. 4, p. 327–337, 1976.

21 SHENG, P.; TIGGELEN, B. van. *Introduction to Wave Scattering, Localization and Mesoscopic Phenomena*. [S.l.]: Taylor & Francis, 2007.

22 ECONOMOU, E.; SOUKOULIS, C. Static conductance and scaling theory of localization in one dimension. *Physical Review Letters*, APS, v. 46, n. 9, p. 618, 1981.

23 BIDEL, Y. et al. Coherent light transport in a cold strontium cloud. *Physical review letters*, APS, v. 88, n. 20, p. 203902, 2002.

24 WILKOWSKI, D. et al. Light transport in cold atoms: the fate of coherent backscattering in the weak localization regime. *Physica B: Condensed Matter*, Elsevier, v. 328, n. 3-4, p. 157–162, 2003.

25 WILKOWSKI, D. et al. Coherent backscattering of light by resonant atomic dipole transitions. *JOSA B*, Optica Publishing Group, v. 21, n. 1, p. 183–190, 2004.

26 SIGWARTH, O. et al. Magnetic field enhanced coherence length in cold atomic gases. *Physical review letters*, APS, v. 93, n. 14, p. 143906, 2004.

27 ARAÚJO, M. O. et al. Superradiance in a large and dilute cloud of cold atoms in the linear-optics regime. *Physical review letters*, APS, v. 117, n. 7, p. 073002, 2016.

28 GUERIN, W.; ARAÚJO, M. O.; KAISER, R. Subradiance in a large cloud of cold atoms. *Physical review letters*, APS, v. 116, n. 8, p. 083601, 2016.

29 BELLANDO, L. et al. Cooperative effects and disorder: A scaling analysis of the spectrum of the effective atomic hamiltonian. *Physical Review A*, APS, v. 90, n. 6, p. 063822, 2014.

30 MAFI, A. Transverse anderson localization of light: a tutorial. *Advances in Optics and Photonics*, Optica Publishing Group, v. 7, n. 3, p. 459–515, 2015.

Appendix

APPENDIX A – Anderson localization for light in 1D system

As an illustration of the phenomenon of Anderson localization, we study the behavior of a particle subjected to a disordered potential inside a one-dimensional box of size $2L$. We analyze and compare the first three eigenvectors, in ascending order of energy, for a potential analogous to a one-dimensional box potential [30]. Our potential depends on position and can be divided into two parts: for positions less than $-L$ or greater than L, the potential is infinite. Between these intervals, the potential is randomly generated and is limited by a maximum amplitude (W). Thus, we analyze how the maximum amplitude of this potential alters the wave function. Therefore, our potential is described as:

$$V(x) = \begin{cases} W\widetilde{V_r}(x), & \text{for} \quad -L < x < L, \\ \infty, & \text{for } x > L \text{ or } x < -L, \end{cases} \tag{A.1}$$

where $\widetilde{V_r}(x)$ is the normalized random potential, meaning that each position (x) is assigned

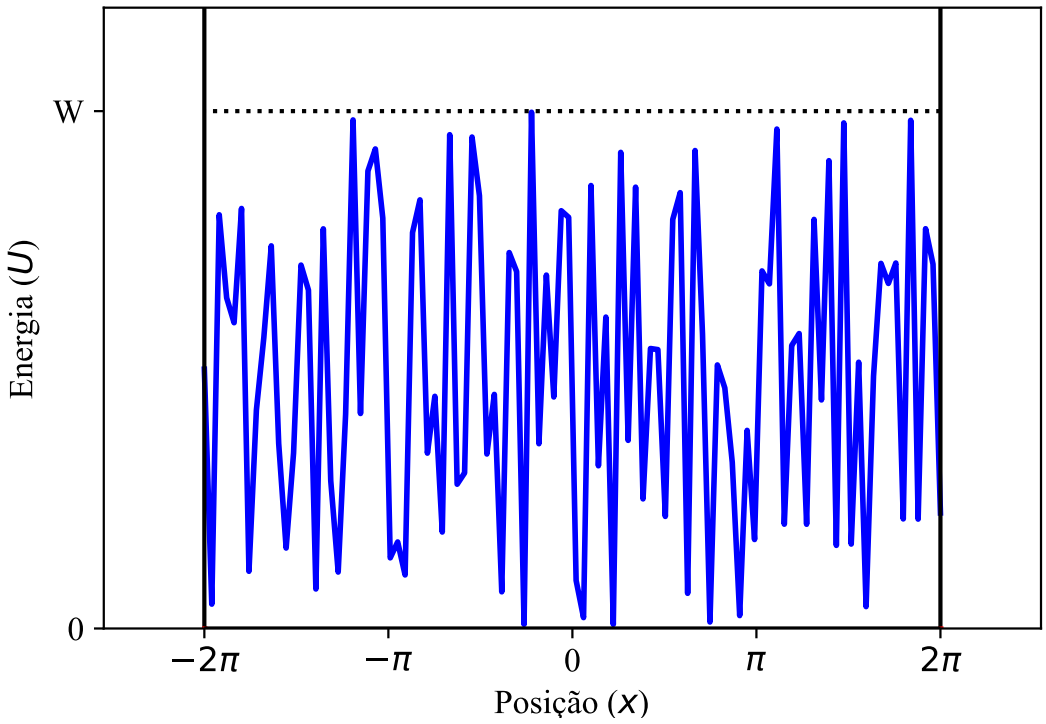

Figure 22 – Normalized random potential represented within the one-dimensional box potential of length $2L$.

a random potential energy value, and W is the maximum amplitude of the potential. To

perform the simulation, we assume $L = 2\pi$, the number of points $N = 100$, and $\hbar = 1$. Additionally, an example of a random potential $\widetilde{V_r}(x)$ is shown in Fig. 22.

The objective of this example is to verify the probability density $|\psi_n|^2$ for different values of the potential amplitude W. We consider four different maximum amplitude values: (a) $W = 10^{-2}$; (b) $W = 1$; (c) $W = 10^2$; and (d) $W = 10^4$. Using the potential $\widetilde{V_r}(x)$ for each case, we compute the Hamiltonians of the particles subjected to these potentials. By extracting the eigenvectors ψ_n and eigenvalues λ_n of the Hamiltonian, we obtain the probability density $|\psi_n|^2$ for finding the particle at position x. The probability density of the first three eigenstates for different amplitudes W is shown in Fig. 23.

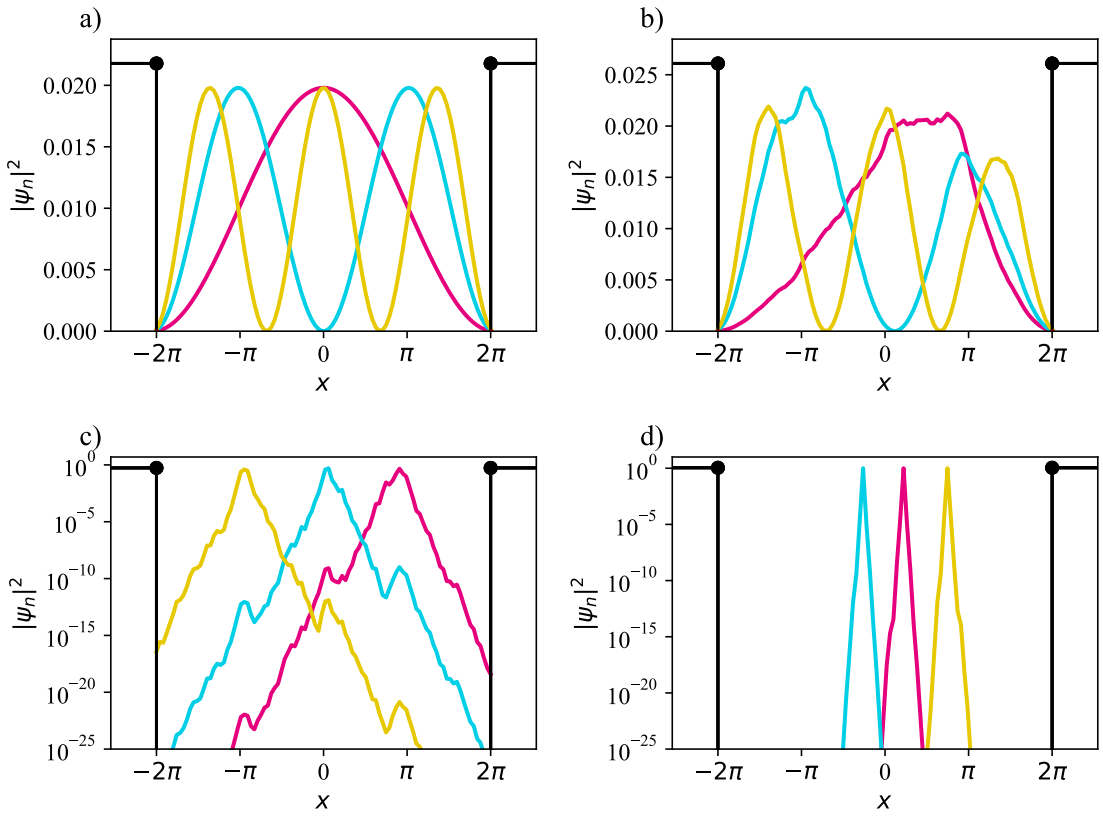

Figure 23 – Probability of finding the particle as a function of position for potential amplitudes $V(x)$ of: (a) $W = 10^{-2}$; (b) $W = 1$; (c) $W = 10^2$; (d) $W = 10^4$. The simulation grid contains 100 points.

In Fig. 23(a) presents the three lowest modes, which are similar to those of a particle in a box of length $2L$ without disorder. In Fig. 23(b), increasing the amplitude W causes a slight alteration in the shape of the modes; for instance, the first mode exhibits a noticeable change in its shape. In Fig. 23(c), the probability density $|\psi_n|^2$ of the first three modes becomes localized near a specific position. We observe that the spatial decay of the modes approaches an exponential behavior, although there are substantial deviations from this profile. Finally, in Fig. 23(d), the probability density is almost entirely concentrated at a single point, clearly exhibiting exponential decay. The spatial decay scale corresponds

to the localization length ξ. For stronger disorder, the localized modes are less affected by finite-size effects due to the shorter localization length. Note that Figs. 23(c) and (d) are presented using a logarithmic scale to highlight the exponential decay. This example demonstrates the implementation of the method and graphically illustrates the concept of Anderson localization. We observed that the localization position of the particle depends on the random potential $\widetilde{V_r}(x)$, i.e., on the amplitude of the disordered component. Finally, all the images and calculations presented in this example were computed using Python and can be found in the author's repository (https://github.com/Fuzit4/Quali).

APPENDIX B – Computational information

The most resource-intensive part of computational calculations is the diagonalization of the interaction matrix between atoms. Based on this, we conducted numerous simulations to verify how each parameter affects both the diagonalization time and the peak memory usage for each simulation. We performed the simulations on two main computers with the following configurations. PC1: CPU: AMD Ryzen 4 4600G with Radeon Graphics, base speed 3.40 GHz; 16 GB of RAM. PC2: CPU: 12th Gen Intel® Core™ i7-12700KF 3.60 GHz; 64 GB of RAM; GPU: NVIDIA GeForce RTX 3050.

In Table 1, the first column represents the number of atoms in the cloud; the second column shows the time, in hours, required to diagonalize the matrix; the third column presents the peak memory usage in gigabytes (GB); and the last column displays the ratio between the time and the cube of the number of atoms. Each row represents one simulation. All simulations in this table were performed on PC1. We used Python for clouds with a density of 0.01 k^2 because we observed that the atomic cloud density does not affect strongly the simulation time and because we are particularly interested in analyzing the vector channel.

Table 1 – Performance under different conditions

Number of Atoms	**Total Time (h)**	**Memory Peak (GB)**	**Time per N^3 (1/h)**
$2.00\ 10^3$	0.02	0.78	$2.25\ 10^{-12}$
$2.00\ 10^3$	0.02	0.78	$2.25\ 10^{-12}$
$4.00\ 10^3$	0.13	3.10	$2.03\ 10^{-12}$
$4.00\ 10^3$	0.13	3.10	$2.03\ 10^{-12}$
$1.00\ 10^4$	1.93	19.37	$1.93\ 10^{-12}$
$1.00\ 10^4$	1.90	19.37	$1.90\ 10^{-12}$

The first observation is that as the number of simulated atoms increases, the diagonalization time also increases. As expected, the time is approximately proportional to the cube of the number of particles. Thus, we define the proportionality constant as the ratio between the diagonalization time and the cube of the number of particles, as presented in the last column. This proportionality constant depends on various factors related to the computer used for the calculations, such as processing speed and other processes running concurrently with the simulation. These factors explain the fluctuation in the proportionality constant. Later in this chapter, we will use these proportionality constants to estimate the time required for a simulation. Finally, the third column shows the memory peak reached during the simulation. This memory peak is significant because if the computer performing the calculations has less RAM than required, it must store

some data on the SSD, and this data transfer significantly increases the code execution time. The memory peak is proportional to the square of the number of particles. One way to reduce this peak is to use the minimum number of variables during the simulation; however, excessively reducing the number of variables can increase the proportionality constant of the execution time. This is a simple example because the atomic radius takes up little memory, but for some variables it can exceed the size of size $(2.50\ 10^4)^2$

In Table 2, we observe the time required to solve the diagonalization problem for two programming languages and for various atomic cloud configurations. All simulations in this table were performed on PC2 because PC1's processor could not compile the Julia programming language. All simulated clouds have a density of 0.01 k^2 and operate in the vector channel.

Table 2 – Comparative Performance Between Python and Julia

Number of Atoms	**Total Time (h)**	**Language**	**Time per N^3**
$2.00\ 10^3$	0.010	Python	$1.13\ 10^{-12}$
$2.00\ 10^3$	0.013	Julia	$1.60\ 10^{-12}$
$4.00\ 10^3$	0.068	Python	$1.03\ 10^{-12}$
$4.00\ 10^3$	0.093	Julia	$1.45\ 10^{-12}$
$1.00\ 10^4$	0.985	Python	$9.70\ 10^{-13}$
$1.00\ 10^4$	1.807	Julia	$1.81\ 10^{-12}$

Thus, Table 2 confirms that the Python simulation is faster than the Julia simulation. For small atomic clouds, the difference in diagonalization time between Python and Julia is relatively minor. However, for the cloud containing $1.0\ 10^4$ atoms, this difference is approximately equal to the entire simulation time for Python. In other words, Python takes half the time to solve the same problem. This difference may be attributed to the Python libraries being more optimized than those available for Julia, a newer programming language. Another notable observation arises when comparing Table 1, which contains all simulations performed in Python, with the Python results in Table 2. This comparison underscores the importance of the computer on which the calculations are performed, as all diagonalization times on PC1 were twice those on PC2.

As discussed earlier, at first we simulated only one realization of a cloud. However, for a more precise conductance calculation, we must average the results. This procedure requires performing the calculation n times for a given cloud size. Additionally, conductance must be calculated for various cloud sizes. Therefore, we must perform these simulations in parallel. To address these challenges, we use the openHPC cluster at UFSCar. More information can be found at https://gitlab.com/ufscar/hpc/documentacao/-/wikis/usuario. The openHPC cluster at UFSCar not only resolves the issue of parallel computation but also overcomes the memory peak limitation, as each machine provides more memory than conventional computers. Thus, Table 3 presents the diagonalization times for simulations

performed on the openHPC cluster at UFSCar for various cloud sizes. Additionally, the third column shows the memory peak used during the simulation.

Table 3 – Performance in Different Configurations

Number of Atoms	**Total Time (h)**	**Memory Peak (GB)**	**Time per N^3**
$2.00\ 10^3$	0.010	0.64	$1.19\ 10^{-12}$
$3.00\ 10^3$	0.090	2.56	$1.28\ 10^{-12}$
$7.75\ 10^3$	0.662	9.62	$1.40\ 10^{-12}$
$1.00\ 10^4$	1.080	16.02	$1.07\ 10^{-12}$
$1.35\ 10^4$	1.908	29.19	$7.26\ 10^{-13}$
$2.00\ 10^4$	9.340	64.08	$1.10\ 10^{-12}$
$2.50\ 10^4$	16.182	100.12	$9.75\ 10^{-13}$
$3.00\ 10^4$	22.460	144.17	$8.22\ 10^{-13}$
$3.50\ 10^4$	46.806	196.23	$1.09\ 10^{-12}$

For small atomic clouds, the diagonalization time on the cluster closely approximates that on PC2. However, when simulating a cloud containing $1.0\ 10^4$ particles, the time required on the cluster doubles that on PC2. Nevertheless, one of the main reasons for using the cluster is its high memory limit, which enables the simulation of increasingly larger clouds. For example, simulating a cloud with $3.5\ 10^4$ atoms takes approximately 26 hours, as shown in the table. From these results, we approximate the proportionality constant relating time to the cube of the number of particles for simulations performed on the openHPC cluster at UFSCar as $1.09\ 10^{-12}$ 1/h. The memory peak can be estimated by squaring the number of particles and multiplying by $1.60\ 10^{-7}$ 1/GB. Using these values, we can estimate the time required for larger matrix calculations and the necessary memory for these matrices.

APPENDIX C – Example Python code

Here is an example Python code that we used for our simulations:

```python
import numpy as np
import matplotlib.pyplot as plt
import random
import time
import math
import matplotlib.ticker as ticker
from scipy.special import hankel1
from matplotlib.patches import Circle
from matplotlib.colors import LogNorm
import matplotlib.patches as patches

# Parameters:
NAtoms = 1000  # Number of atoms
channel = 0    # Channel: 0 (scalar), 1 (vectorial)
rho = 1        # Cloud density

R = np.sqrt((NAtoms / rho) / np.pi)  # Calculates the cloud's radius
print(f"\r Radius: ({R:.2f})", end='')

# Generating the cloud in random coordinates
x = 2 * R * (np.random.rand(NAtoms) - 0.5)
y = 2 * R * (np.random.rand(NAtoms) - 0.5)

# Ensuring that atoms are within the cloud radius
for j in range(NAtoms):
    while np.sqrt(x[j]**2 / R**2 + y[j]**2 / R**2) > 1:
        x[j] = 2 * R * (np.random.rand() - 0.5)
        y[j] = 2 * R * (np.random.rand() - 0.5)

# Visualization of the atoms
plt.scatter(x, y, color='blue')
circle = Circle((0, 0), R, color='black', fill=False, linestyle='--',
↪  linewidth=2)
plt.gca().add_patch(circle)
plt.xlabel('x')
plt.ylabel('y')
```

```
36 plt.title('Atoms inside the cloud')
37 plt.grid(True)
38 plt.axis('equal')
39 plt.show()
40
41 # Distances between pairs of atoms
42 xij = np.outer(x, np.ones(NAtoms)) - np.outer(np.ones(NAtoms), x) +
   ↪  np.eye(NAtoms)
43 yij = np.outer(y, np.ones(NAtoms)) - np.outer(np.ones(NAtoms), y) +
   ↪  np.eye(NAtoms)
44
45 # 2D distance
46 dij = np.sqrt(xij**2 + yij**2)
47 phiij = np.arctan2(yij, xij)
48
49 # Auxiliary matrix
50 aux = np.ones((NAtoms, NAtoms)) - np.eye(NAtoms)
51
52 # Scalar kernel matrix
53 gamma00 = np.eye(NAtoms) + aux * hankel1(0, dij)
54
55 # Checks if the channel is vectorial (1) or scalar (0)
56 if channel == 1:
57     hankel2 = aux * hankel1(2, dij)
58     gammaMP = -np.exp(2j * phiij) * hankel2
59     gammaPM = -np.exp(-2j * phiij) * hankel2
60     Gamma = np.block([[gamma00, gammaMP], [gammaPM, gamma00]])
61 else:
62     Gamma = gamma00
63
64 # Diagonalization
65 diag_time = time.time()
66 e_vec_0, v_vec0 = np.linalg.eig(Gamma)
67 diag_elapsed_time = time.time() - diag_time
68 print(f'It took {diag_elapsed_time:.3f} seconds to diagonalize the matrix')
69
70 # Memory cleanup
71 dij, phiij, aux, hankel2, gammaMP, gammaPM = [None] * 6
72
73 # Extracting the real and imaginary parts of eigenvalues
74 Gamma_real = np.real(e_vec_0)
```

```
Gamma_imag = np.imag(e_vec_0)

# Filtering for real eigenvalues above a threshold
threshold = 1e-2
mask = Gamma_real > threshold
Gamma_14_np = Gamma_real[mask]
omega_14_np = Gamma_imag[mask] if len(Gamma_imag) > 0 else np.array([])
autovec_14_np = v_vec0[:, mask] if len(v_vec0) > 0 else np.array([])

# IPR calculation
def ipr(eigenvector):
    return sum(np.abs(eigenvector)**4) / (sum(np.abs(eigenvector)**2)**2)

ipr_n = np.array([ipr(autovec) for autovec in autovec_14_np.T])

# Spectrum visualization
fontsize_value = 40
fontsize_value_solo = fontsize_value - 20

fig, axs = plt.subplots(1, figsize=(13, 10))
scatter = axs.scatter(omega_14_np, Gamma_14_np, c=ipr_n, cmap='viridis',
↪  s=200, norm=LogNorm())
cbar = fig.colorbar(scatter, ax=axs)
cbar.set_label('IPR', fontsize=fontsize_value_solo)
axs.set_xlabel('', fontsize=fontsize_value_solo)
axs.set_ylabel('', fontsize=fontsize_value_solo)
axs.set_yscale('log')
axs.tick_params(axis='both', labelsize=fontsize_value_solo)
cbar.ax.tick_params(labelsize=fontsize_value_solo)
plt.show()


```